Nanocrystal Residual Strains and Density Layers Enhance Failure Resistance in the Cleithrum Bone of Evolutionary Advanced Pike Fish

Katrein Sauer, Andreia Silveira, Vanessa Schoeppler, Alexander Rack, Ivo Zizak, Alexandra Pacureanu, Nadine Nassif, Ioanna Mantouvalou, Wout de Nolf, Claudia Fleck, et al.

HAL Id: hal-04520748
https://hal.sorbonne-universite.fr/hal-04520748

Submitted on 18 Jun 2024

Journal Pre-proof

Nanocrystal Residual Strains and Density Layers Enhance Failure Resistance in the Cleithrum Bone of Evolutionary Advanced Pike Fish

Katrein Sauer , Andreia Silveira , Vanessa Schoeppler , Alexander Rack , Ivo Zizak , Alexandra Pacureanu , Nadine Nassif , Ioanna Mantouvalou , Wout de Nolf , Claudia Fleck , Ron Shahar , Paul Zaslansky
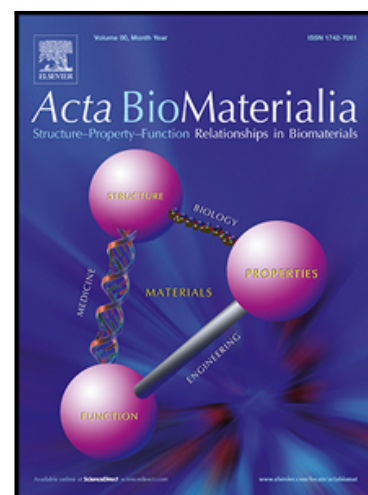
Please cite this article as: Katrein Sauer , Andreia Silveira , Vanessa Schoeppler , Alexander Rack , Ivo Zizak , Alexandra Pacureanu , Nadine Nassif , Ioanna Mantouvalou , Wout de Nolf , Claudia Fleck , Ron Shahar , Paul Zaslansky , Nanocrystal Residual Strains and Density Layers Enhance Failure Resistance in the Cleithrum Bone of Evolutionary Advanced Pike Fish, *Acta Biomaterialia* (2024), doi: https://doi.org/10.1016/j.actbio.2024.03.017

Nanocrystal Residual Strains and Density Layers Enhance Failure Resistance in the Cleithrum Bone of Evolutionary Advanced Pike Fish

Katrein Sauer [a,*], Andreia Silveira [a], Vanessa Schoeppler [b], Alexander Rack [c], Ivo Zizak [d], Alexandra Pacureanu [e], Nadine Nassif [f], Ioanna Mantouvalou [g], Wout de Nolf [c], Claudia Fleck [h], Ron Shahar [i], Paul Zaslansky [a,*]

[a,*] K. Sauer, Charité - Universitätsmedizin Berlin, Department for Operative, Preventive and Pediatric Dentistry, Aßmannshauser Straße 4-6, 14197 Berlin, Germany, email: katrein@physik.hu-berlin.de, phone: (+49) 30 450 562235

[a] A. Silveira, Charité - Universitätsmedizin Berlin, Department for Operative, Preventive and Pediatric Dentistry, Aßmannshauser Straße 4-6, 14197 Berlin, Germany, email: andreia.sousa-da-silveira@charite.de, phone: (+49) 30 450 562235

[b] V. Schoeppler, Henry Royce Institute, Department of Materials, University of Manchester, Manchester M1 3BB UK, email: vanessa.schoeppler@gmail.com; (+49) 30 450 562235

[c] A. Rack, ESRF – The European Synchrotron Radiation Facility, 71 Av. des Martyrs, 38000, Grenoble, France, email: rack@esrf.fr, phone: (+33) 476 88 1781

[d] I. Zizak, Helmholtz-Zentrum Berlin, Department for Structure and Dynamics of Energy Materials (SE-ASD), Albert-Einstein-Straße 15, 12489 Berlin, Germany, email: zizak@helmholtz-berlin.de, phone: (+49) 30 8062 12127

[e] A. Pacureanu, ESRF – The European Synchrotron Radiation Facility, 71 Av. des Martyrs, 38000, Grenoble, France, email: pacureanualexandra@gmail.com, phone: (+33) 4 76 88 17-27

[f] N. Nassif, Laboratoire Chimie de la Matière Condensée de Paris, Ecole Pratique des Hautes Etudes, University Pierre and Marie Curie-Paris 6, Paris, France, email: nadine.nassif@sorbonne-universite.fr, phone: Tel: +33 1 44 27 63 22

[g] I. Mantouvalou, Helmholtz-Zentrum Berlin für Materialien und Energie, Hahn-Meitner-Platz 1, 14109 Berlin, Germany, email: ioanna.mantouvalou@tu-berlin.de, phone: (+49) 30 314 79057

[c] W. de Nolf, ESRF – The European Synchrotron Radiation Facility, 71 Av. des Martyrs, 38000, Grenoble, France, email: wout.de_nolf@esrf.fr, phone, (+33) 4 76 88 21-54

[h] C. Fleck, University of Technology Berlin, Materials Science & Engineering, Str. des 17. Juni 135 - Sekr. EB 13, 10623 Berlin, Germany, email: claudia.fleck@tu-berlin.de, phone: (+49) 30 314 23605

[i] R. Shahar, Koret School of Veterinary Medicine, The Robert H. Smith Faculty of Agriculture, Food and Environment, Hebrew University of Jerusalem, Rehovot, 76100, Israel, email: ron.shahar1@mail.huji.ac.il, phone: (+972) 08 9489756

[a,*] P. Zaslansky, Charité - Universitätsmedizin Berlin, Department for Operative, Preventive and Pediatric Dentistry, Aßmannshauser Straße 4-6, 14197 Berlin, Germany, email: paul.zaslansky@charite.de, phone: (+49) 30 450 662215

Abstract

Failure-resistant designs are particularly crucial for bones subjected to rapid loading, as is the case for the ambush-hunting northern pike (Esox lucius). These fish have slim and low-density osteocyte-lacking bones. As part of the swallowing mechanism, the cleithrum bone opens and closes the jaw. The cleithrum needs sufficient strength and damage tolerance, to withstand years of repetitive rapid gape-and-suck cycles of feeding. The thin wing-shaped

bone comprises anisotropic layers of mineralized collagen fibers that exhibit periodic variations in mineral density on the mm and micrometer length scales. Wavy collagen fibrils interconnect these layers yielding a highly anisotropic structure. Hydrated cleithra exhibit Young's moduli spanning 3-9 GPa where the yield stress of ~40 MPa increases markedly to exceed ~180 MPa upon drying. This 5x observation of increased strength corresponds to a change to brittle fracture patterns. It matches emergence of compressive residual strains of ~0.15% within the mineral crystals due to forces from shrinking collagen layers. Compressive stresses on the nanoscale, combined with the layered anisotropic microstructure on the mm length scale, jointly confer structural stability in the slender and lightweight bones. By employing a range of X-ray, electron and optical imaging and mechanical characterization techniques, we reveal the structure and properties that make the cleithra, naturally grown, damage resistant composites.

List of Abbreviations

cAP = carbonated apatite
CC = caudiocranial
DIC = digital image correlation
DV = dorsoventral
DVT = digital volume tomography (DVT)
EDX = energy dispersive X-ray spectroscopy
PCE-μCT = phase contrast-enhanced micro-Computed Tomography
PD = proximodistal
PLM = polarized light microscopy
SEM = scanning electron microscopy
TGA = thermogravimetric analysis
XRD = X-ray diffraction
XRDo-μCT = X-ray diffraction orientation micro-ComputedTomography
μCT = micro-Computed Tomography
μ-indentation = micro indentation

1. Introduction

Bone material, the stiff tissue found in most vertebrates, is a hierarchical biocomposite with different characteristics revealed at nanometer, micrometer, and millimeter length scales of observation [1–3]. Through lengthy natural selection, bones have evolved to exquisitely utilize both material composition and geometry to create functionally adapted structures. They are composed primarily of two nanoscale components: type I collagen fibrils (50~200 nm in diameter) and carbonated apatite (cAP) mineral nanocrystal plates (~50 x 25 x 5 nm) [3–5]. The organic and inorganic components are packed into mineralized collagen fibrils, bundles which form larger assemblages organized into various geometries and lamellae (that are further shaped e.g. into plates and spines). The manner in which bone is arranged at the nanometer length scales, with gradients in mineral content, as well as three-dimensional fibril texturing, is believed to be a result of adaptation to the mechanical environments in which each bone operates [3,6].

Bones serve as light-weight yet strong protective casings in widely differing situations, for example, in the mammalian skull where the cortex is x40 stronger than the normal loads to which it is exposed [7]. Some bones offer very high impact resistance, for example deer antlers [6,8]. Bone as a material has been shown to excellently resist crack propagation, which is important to prevent functionally-catastrophic fracture [1,9,10]. The high toughness [11] emerges from intrinsic and extrinsic toughening mechanisms [12] that either increase the

resistance to crack growth or reduce the stresses that act to drive the crack forward [10,12]. Both strength and enhanced toughness are needed for bones to sustain the stress-raising effects of inclusion of blood vessels and pores [13].

Bones are living biological tissues, and they respond to external loads via mechanosensation. Bone re/modeling, the reactive process of adding and/or removing bone material, has been extensively researched [14]. When parts of the skeleton are exposed to repeated loads, biochemical cascades are triggered, with osteoclast cells removing certain domains while osteoblasts produce new material that enlarges or strengthens the structure, thus adapting it to external stresses [15,16]. Adaptation by remodeling in mammals results in self-repair and renewal, which is believed to be orchestrated by osteocytes, cells that reside within small oval-shaped cavities (~10 x 5 x 5 μm) known as lacunae. The cells in such lacunae are interconnected through a lacunocanalicular network, which consists of small canalicular channels 200~300 nm in diameter [17,18]. It is widely assumed that this network is responsible for initiating and mediating the adaptation process in which old bone is removed (resorption) while new bone material is created (deposition).

However, not all bones have osteocytes, as observed in neoteleosts, a major group of fish considered to be evolutionarily advanced. Indeed, in such anosteocytic bones (i.e. bones without osteocytes) of species such as medaka, tilapia, swordfish, and marlins [19–23] remodeling has been observed, despite a complete absence of osteocytes [24,25]. We previously showed how remodeling occurs in the attachment hinges of the repeatedly loaded cleithrum bones of the pectoral girdle [26] (*Esox Lucius,* see Supplementary Fig. 1 and SI Video 1). The lack of osteocytes suggests that cells in the matrix cannot play a role in bone remodeling and normal bone maintenance. At the same time, the elongated flat cleithra bones play crucial roles in enabling repeated swift mouth and pharynx mobilization (Fig. 1A and Supplementary Fig. 1). Cleithra are mechanically loaded by strong muscles that the fish activates when the animal quickly ingests food. This bone is essential for ambush-capturing and swallowing of prey using a "gape-and-suck" method [27] (see SI Video 2). Yet, it is not known if the bones become damaged during function, and if they do, what mechanisms might foster damaged bone replacement. In any case, for the fish to survive, these bones must never fail.

To open the mouth rapidly, the pike uses the cleithra on both sides of the head as levers [26,28,29]. They are actuated by muscles that generate swift backward pull (depicted in Fig. 1A by the yellow arrow) directing forces along a craniocaudal principal axis of the fish body (highlighted in purple). It is estimated that such activation takes place within ~0.03 seconds [27,30] which is mechanically challenging, because the mouth gape must rapidly accelerate a large volume of water containing the prey (see SI Video 2). To do so, significant stresses need to be sustained by the loaded cleithrum bones [28,29]. These same bones also anchor the pectoral fins proximally, as they emerge ventrally, to act as stabilizers while participating in precision fish swim maneuvers. The fins emerge from below, and are connected to the cleithrum. The cleithrum thus forms a mechanical basis for the fins to propel large volumes of water. Pike slowly position themselves in the water, and when needed, there are reported instantaneous acceleration rates exceeding 240 m s^{-2} [28,29]. The cleithrum must therefore sustain repeated load cycles while moving rapidly along its long, principal axis, yet little is known about the bone structure and the accompanying mechanical characteristics.

In this study, we characterize bones extracted from wild-caught northern pike, to explore what structural attributes of the cleithra make them well adapted to withstanding repeated loading *in vivo*. We determine the chemical, textural and mechanical properties at multiple hierarchical levels of organization. Mechanical testing techniques at the cm-mm length scale are accompanied with nanocrystal strain measurements at the Å length scale. These are related to structure revealed by complementary-contrast optical electron and X-ray 2D and

3D imaging techniques. We observe that regionally-varying nanocrystal residual stresses at different distances from the outer bone regions help to establish an impressively resilient anosteocytic bone, designed for high-cycle, repeated-load, fail-safe function. This work shows how cleithra comprise smart composite structures that help make the northern pike a widely distributed successful freshwater hunter.

2. Materials and Methods

2.1 Sample preparation

Cleithrum bone samples were obtained from recently caught *Esox lucius* pike fish, (Fig. 1A and Supplementary Fig. 1), purchased from local fish markets in Berlin, Germany, over 5 years. In each head (n=10) both left and right cleithrum samples were dissected and stored wet. Segments of some of the cleithrum were cut into beams (~1 x 1 x 20 mm^3) while others were cut into cubes (~1 x 1 x 1 mm^3) using a slow-speed precision water-cooled saw (IsoMet, Buehler, ITW Test, and Measurement GmbH, Düsseldorf, Germany) equipped with a wafering diamond blade. The cleithra orientations with respect to the pike anatomy are depicted in Figs. 1A and B.

2.2 Digital volume tomography (DVT) – clinical X-ray cone beam tomography

A particularly large single pike fish head (>10 kg catch) was imaged using a SIRONA (OrthoPhos) Galileos Comfort Plus CT – Dental X-ray machine (SIDICOM RM version 3.7). The resulting digital volume tomography scan reconstruction had voxel sizes of 0.288 mm^3. The data were processed using Fiji [31] for cropping, reorienting, enhancing contrast and visualization of the skull and fins with the soft tissue intact.

2.3 Laboratory computer tomography (µCT)

Entire cleithra (n=10) were first scanned whole at low (20 µm) resolution, thereafter used to cut bars (n=16) that were then scanned using a lab-based µCT system (Skyscan 1172, Brucker-microCT, Kontich, Belgium) at higher (6 µm) resolution. Scans were conducted using a source energy of 80 kV and a current of 124 µA and reconstructed using NRecon software (Version 1.7.0.3) and visualized using Fiji [31].

2.4 Synchrotron-radiation-based tomography: absorption versus phase contrast enhanced

15 bar-shaped cut-out bone samples were scanned by absorption and by phase contrast enhanced micro-computed tomography (PCE-µCT) [32] at beamline ID19 of the European Synchrotron Radiation Facility (ESRF), Grenoble, France. Data were collected with a pink beam photon energy of 34 keV and an image voxel size of 0.65 µm. For absorption contrast, samples were imaged at a 14 mm sample detector distance. For PCE-µCT, inline phase contrast enhancement was used by employing a propagation distance of 91 mm between the sample and detector. The large data sets (>4000 projections) were reconstructed using the open-source code PyHST2 [33]. A single-distance phase-retrieval algorithm was used for reconstruction of the phase contrast-enhanced data using a delta-beta parameter ratio of 500, similar to previous reports [26,34].

Mass density was estimated from 15 samples measured in absorption mode based on calibration with two phantoms of known mineral density (0.25 and 0.75 mg cm^{-3}). Regions of higher and lower density within the reconstructed data were identified and evaluated.

2.5 High-resolution phase contrast-enhanced nanotomography (nano-CT)

Nanotomography was performed in cut-out beam samples (n=3) at the ID16A-NI nano-imaging beamline of the ESRF [35] (Grenoble, France). A high-brilliance coherent X-ray beam with a photon energy of 17 keV was used while the samples were mounted on a rotation stage inside the beamline vacuum chamber. The illumination source was a set of multilayer-coated mirrors (Kirckpatrick-Baez crossed mirror geometry) [36]. The samples were scanned with voxel sizes of either 120 nm or 25 nm, at multiple distances with 2000 projections each. For further details see SI, *1. Materials and Methods, 1.1.*

2.6 Scanning electron microscopy (SEM)

Cleithra from 6 pikes and one sturgeon fish, as well as one mouse tibia were prepared for fracture surface observation by electron microscopy. Three of the cleithra were fractured under wet conditions while all other bones were fractured dry, following air drying under ambient conditions. The fracture surfaces were imaged uncoated using scanning electron microscopy (SEM, PhenomXL, ThermoFisher, Eindhoven, Netherlands) in backscatter imaging mode at 10 kV and 15 kV. Other samples were used for mass density and chemical composition analysis following dehydration. In such measurements, elongated cut beams were ground and polished using laboratory grinding and polishing machines with diamond suspension grain sizes of 9 μm, 3 μm, 1 μm, and 0.25 μm. Two (n=2) samples were dehydrated in increasing concentrations of ethanol (50 %, 70 %, 90 %, and 100 %) followed by critical point drying in acetone (CPD 030, BAL-TEC, Balzers, Liechtenstein). These samples were carbon coated (MED010 Balzers coater, Wiemer EM-Service OHG, Wetter, Germany) and imaged using a high-vacuum MaXim SEM (CamScan, Cambridge, UK) in secondary imaging mode at an energy of 15 keV. Energy-dispersive X-ray (EDX) spectra were collected with a QUANTAX EDS XFlash 6130 system (Bruker Nano GmbH, Berlin, Germany). EDX maps were scanned at an acceleration voltage of 20 kV using a dwell time of 256 μs, a line average of 8 with a spot size of ~1 μm. Spectra were processed (Esprit 2.0, Bruker QTX, Berlin, Germany) to create maps of calcium (Ca), phosphorus (P), and carbon (C). Air dried samples (n=2) were imaged using the SEM (PhenomXL, ThermoFisher, Eindhoven, Netherlands) in backscatter imaging mode at 20 keV to determine mass density by comparison to bovine enamel with known mineral content.

2.7 Second harmonic generation (SHG) confocal laser scanning microscopy

Sections of cleithra beams (n=11) were imaged to visualize the orientation and distribution of collagen fibrils along all 3 anatomical directions of the fish (Fig. 1A). Backscattered second harmonic generation (SHG) imaging was performed using a Leica TCS SP5II confocal laser scanning microscope (Leica Microsystems GmbH, Wetzlar, Germany). The SHG signal was generated using a Spectra Physics Ti: sapphire laser (Mai Tai HP, Spectra Physics, Santa Clara, CA, U.S.A.) with 100 fs pulse width at 80 MHz and wavelength of 910 nm with a pinhole of 600 μm. A water immersion lens (HCX IRAPO L 25.0 x 0.95) was used to image the samples wet, with a lateral resolution of ~600 nm and depth steps of ~1 μm. Further details are provided in SI, *1. Materials and Methods, 1.2.*

2.8 Polarized light microscopy

To validate observations by SHG and collagen distributions, one bone bar of cut cleithrum bone was demineralized for cross-polarized optical microscopy analysis [37]. Following standard processing protocols, the sample was decalcified by immersion in EDTA for nine days with solution changes every three days, followed by dehydration in a graded series of ethanol solutions using an automatic tissue processor (Leica TP1020, Leica Biosystems Nussloch GmbH, Nussloch, Germany). The decalcified samples were then embedded in paraffin and cooled for slicing using a microtome (LEICA RM2235, Leica Biosystems

Nussloch GmbH, Nussloch, Germany) to produce 5 µm thick slices. These were subsequently deparaffined with Xylol and rehydrated in a descending alcohol series starting at 100 %, 96 %, 80 %, and 70 % in preparation for staining. Picrosirius red powder (Direct Red 80, Sigma - Aldrich 365548) was dissolved in Picric acid and flushed with acetic acid, ethanol, and Xylol. The slices were placed on microscope cover glasses and coated with mounting media (Vitro-Clud, R. Langenbrick GmbH, Labor- und Medizintechnik, Emmendingen, Germany). Observations were performed using a transmission Zeiss AxioImager A2 POL equipped with standard accessories using a Zeiss 10x0.25 Pol objective for examining birefringent samples under polarized light (crossed polarization and a quartz first-order retardation plate) and an AxioCam CCD camera.

2.9 Synchrotron-based X-ray diffraction (XRD)

X-ray diffraction measurements were performed at the mySpot beamline of the BESSY II synchrotron light source (HZB- Helmholtz-Zentrum, Berlin, Germany). Each sample was measured wet and then measured again following standardized dehydration. The samples (n=5) ground to produce even slabs using silicon carbide grinding paper (4000 grit) to reach a size of approximately 500 x 300 x 3000 μm^3 after which the samples were stored moist. At all stages of preparation, the samples were maintained fully hydrated.

For diffraction measurements, the samples were mounted in PTFE film to maintain hydration. XRD scanning was performed with an energy of 18 keV, sample-to-detector distances of ~345 mm (multiple experiments with small differences), and an X-ray beam size of ~20 µm. Diffraction patterns were collected using a 3269 x 3110 pixel Dectris M9 Eiger detector with a lateral pixel size of 75 µm. The detector orientation, rotation, and sample-to-detector distance were calibrated using powdered corundum (Al_2O_3, grains <50 µm). The calibrants were placed on the PTFE film directly on both sides of each sample. After wet-state diffraction measurements, each sample was dehydrated in an oven at 120 °C for 1 hour and was then re-measured alongside the calibrants. For both the wet and dry states, a series of diffraction images were obtained with lateral steps of approximately 40 µm. The samples were scanned at 25 different heights in which line scans were acquired in non-overlapping points, using exposures of 10 s across the entire sample cross-section. The software package XRDUA (version 6.5.3.1 64bit [38]) was used to convert the diffraction patterns into integrated line profiles of the (002) reflection corresponding to the c-lattice parameter of cAP mineral. For further details on strain calculation and mass density estimation [39] see SI, *1. Materials and Methods, 1.3.*

2.10 Nanocrystal orientation by X-ray diffraction micro-tomography (XRDo-µCT)

Diffraction tomography scans were collected for 3 pike-bone pin-shaped samples with approximate dimensions of ~500 x 300 x 3000 µm in size. The samples were cut along a craniocaudal orientation, produced by grinding with silicon carbide grinding paper (4000 grit) and were allowed to air dry. After mounting upright on the mySpot beamline rotation stage (SmarAct rotation motor, SmarAct GmbH, Oldenburg, Germany), the samples were measured in air, as follows. A diode was used to locate the samples prior to the XRDo-µCT measurements. Both transmission and diffraction scans were collected at multiple sample heights. Each height was scanned at different non-overlapping points by moving the sample both laterally and along the long sample axis, while rotating the sample with incremental angles of 10° up to 180°. Each point was irradiated for 10 s, sufficient to collect (002)-reflections in clearly visible arcs on the Eiger detector. For further details see SI, *1. Materials and Methods, 1.4.*

2.11 X-ray fluorescence - micro-computed tomography (XRF-µCT)

X-ray fluorescence (XRF) spectra were obtained concomitantly during the XRD measurements. Fluorescence multi-channel analysis (mca) files were collected using a Röntec X-Flash (1201/Bruker) detector with a window area of 3 mm^2, mounted at 45° to the incident beam direction. The XRF sample-to-detector distance was 30 mm. The intensities of peaks corresponding to calcium (Ca), zinc (Zn) and strontium (Sr) were transformed into sinograms and converted into fluorescence tomography reconstructed slices, similar to the XRD-μCT orientation data.

2.12 Quantitative laboratory X-Ray fluorescence (lab-based XRF) spectrometry

Geometry calibrated XRF maps were collected to quantify mainly P, Ca and Zn levels, based on measurements from cleithrum bone samples with approximate dimensions of ~150 x 500 x 2000 μm^3. Each sample was mounted within a modified micro-XRF spectrometer (Bruker, M4 Tornado, Bruker AXS GmbH, Karlsruhe, Germany) to scan full X-ray fluorescence maps at 50 kV with a source current of 1mA. For further details see SI, *1. Materials and Methods, 1.5.*

2.13 Thermogravimetric analysis (TGA)

Thermogravimetric analysis (TGA) was performed on cleithrum samples (n=9) from 6 different pikes, saturated in ethanol 70%, followed by immersion in acetone for defatting, using an AQ500 thermo gravimetric analyzer (TA Instruments, Waltham, MA). The average weight of the samples was 3.3 ± 0.4 mg at the start of the experiment. Weight loss was measured as a function of temperature that increased from 25°C to 650°C/min at a rate of 10 °C/min. The analysis software (Thermal Advantage (TA) (version 4.5A, TA Instruments, Waters LLC, New Castle, DE)) was used to run the experiment, and the data were evaluated using the Universal Analysis (UA) module.

2.14 Mechanical characterization - Three-point bending tests

Dehydrated beams (n=3), with approximate dimensions of ~1 x 1 x 20 mm^3, were examined to investigate the strength of bone in three-point bending experiments using a Bose Test Bench LM 1 ElectroForce (Bose, Eden Prairie, MN) equipped with 225 N load cell. We ensured that the geometry of the experiments (thickness of beam vs distance between supports) is at least 1:15 to gain valid results [40]. The bones were positioned for bending tests with a 10 mm distance between the end supports. Force and displacement data were recorded at a frequency of 100 Hz with load applied at a strain rate of 0.3 s^{-1}.

Hydrated cleithrum beams (n=28), obtained from four different fish with approximate dimensions of ~1 x 1 x 20 mm^3, were used for three-point bending tests measured using a custom-built loading machine in which a moving anvil with a single prong was attached to a load cell (model 31, Sensotec, Columbus, OH, USA), moved by a high-precision linear motor (Physik Instrumente (PI) GmbH, Karlsruhe, Germany). The mechanical tests were conducted with the samples submerged in saline solution, with the distance between sample supports of length L = 10 mm. The load (10 N load cell) and displacement data were collected by custom-written software (LabView, National Instruments, Austin, TX, USA) at increasing forces (at a frequency of 50 Hz) at a strain rate of 0.2 s^{-1}. For further details see SI, *1. Materials and Methods, 1.6.*

2.15 Micro-indentation

Elastic modulus of the bone specimens was also estimated based on indentation of hydrated samples (n=12) in both cube (~1 x 1 x 1 mm^3) and beam geometries (~1 x 1 x 20 mm^3) obtained from four different fish. Surfaces on these samples were prepared for

microindentation by grinding and polishing with silicon carbide paper (4000 grit) and diamond suspensions (grain sizes: 3 µm and 1 µm) used on cloth. The samples were then fixed horizontally wet using dental acrylic resin (Temporary Resin Acrylic-Powder mixed with liquid, Bosworth, Skokie, USA) to facilitate reproducible hydrated measurements in the micro-indenter (Future-Tech, microhardness tester, FM-300, NY, USA) equipped with a Vickers tip. Conventional HV values were obtained using standard measurements of each indent. Each sample, continuously hydrated, was indented at room temperature using 10 gram force (gf) applied for 10 seconds. A minimum of 30 indents were made for each sample on the exposed surfaces of the three anatomical orthogonal orientations. The distance between neighboring indents was >2.5 times the actual diagonal indent length. For further details see SI, *1. Materials and Methods, 1.7.* The HV values obtained are provided in the SI section.

2.16 Bulk compression elastic testing with optical strain analysis by digital image correlation (DIC)

Cuboidal bone samples (n=22, ~1 x 1 x 1 mm^3) were cut out of hydrated cleithra of 4 pike fish. Compression tests were conducted using a custom-made mini mechanical tester (OWIS L-Step 22/2, Staufen, Germany) equipped with a 222 N load cell model 31(RDP Electronics, Wolverhampton, UK). The samples were loaded at a crosshead displacement rate of 0.5 µm/s and forces were measured up to a total force of 25 N, well below the expected yield point, monitored while collecting images for DIC analysis [41]. Different samples were used so that deformation was determined on exposed surfaces along the three anatomical orthogonal orientations (Fig. 1). Imaging was performed using a 3D Leica DVM2500 digital microscope with a 320x objective. The samples were fixed to the anvils using a high-stiffness (E > 10 GPa) light-cured dental restorative Z100 MP to ensure contact between the samples and the load supports. Each mounted sample was loaded in five consecutive loading cycles at room temperature. Deformation along and across the observed surfaces was analyzed using digital image correlation performed using the commercial software Vic-2D [42,43], which generated on-axis and orthogonal displacement maps that were then converted into strain from gradients determined using Matlab v. 2015 (math works, USA). The slopes of the linear section of the resulting stress-strain curves were used to determine Young's modulus for each orientation [41,42].

2.17 Statistical analysis

For reported mass density and ash weight values mean and standard deviation were determined with Gnumeric Spreadsheet (Version 1.12.17, 1998-2014).

For Hardness Vickers (HV) and Young's moduli values median values and standard errors were calculated using Gnumeric software. A comprehensive 3D bar plot summarizing the median values and their respective standard deviations shown as error bars from all mechanical testing methods was generated using RStudio version 1.1.453.

Average crystal lattice parameter distribution with shaded standard deviation was analyzed by descriptive statistics using RStudio and Gnumeric software.

A histogram depicting the anisotropy intensity ratios between on-/off-axis orientations for all measured points was generated using SciDavis version 2.3.0.

3. Results

3.1 Typical pike fish cleithrum morphology and texture

The cleithrum is a flat, double-curved, elongated wing-shaped bone, as revealed by low-resolution clinical digital volume tomography (DVT) (Fig. 1B, top) and high resolution μCT (Fig. 1B, bottom and Supplementary Video 1).
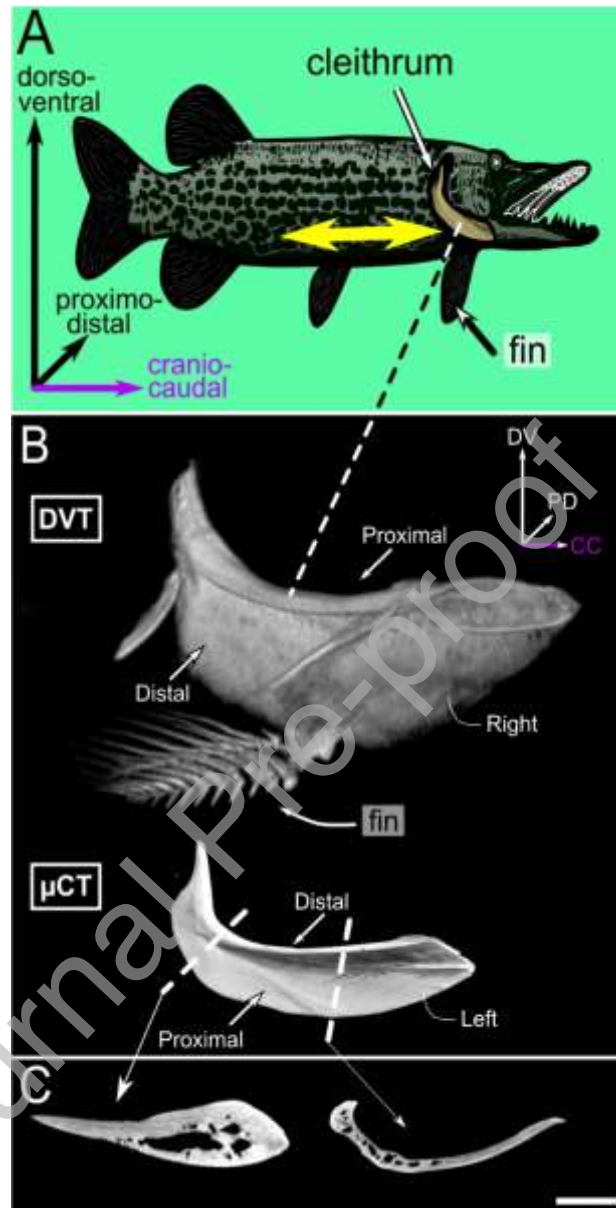

Figure 1: Macroscopic views of the cleithrum bone of pikes (Esox lucius). (A) A schematic of a pike fish illustrates the loading direction of the cleithrum during fast mouth opening, indicated by the yellow arrow. The coordinate system corresponds to the anatomical axis of the pike fish body: dorsoventral (DV), proximodistal (PD), and craniocaudal (CC). **(B)** Clinical digital volume tomography (DVT, top) and μCT (bottom) renderings of the flat and wing-shaped right cleithrum along its craniocaudal principal orientation (highlighted in purple). The DVT allowed us to image the bones and fins still within the intact pike head. White dashed lines in μCT rendering indicate the anatomical positions of the left cleithrum. **(C)** The μCT cross-sections of the cleithrum (origin indicated by white arrows) reveal a compact bone near the hinge of the cleithrum, pervaded with channel-like cavities (left image). The dense half of the bone is found in the region supporting the fins, appearing homogeneous without pores. The scale bar length in C is 0.5 cm.

All cleithra are made of thicker domains on the dorsal side with large internal marrow-containing voids. The ventral and much of the caudal regions are thin, appearing macroscopically uniform and compact. In one such region, highlighted in Fig. 1B (top), the bone forms a ledge that supports the pectoral fins (Fig. 1A, B and Supplementary Fig.1). Cross-sections showing the compact and the thicker bone domains are presented in Fig. 1C. Comparative scanning electron microscopy (SEM) images demonstrate the structural differences between anosteocytic cleithra of pikes (Fig. 2A.1), as compared with cleithra of osteocytic sturgeon fish (Fig. 2B.1) and osteocytic mouse femora (Fig. 2C.1). White arrowheads showcase typical osteocytic lacunae exhibiting the characteristic shape of such cavities [25,44,45] in sturgeon and mouse bones, with close-ups shown in A.2, B.2, and C.2. In pike, close-ups reveal a fibrous granular extracellular matrix of mineralized collagen fibers lacking osteocytes. The same lack of osteocytes is observed in the bulk of the bone observed by high resolution PCE-μCT data (e.g. SI Figure 2). Note how in mouse bone (C.2) a typical canaliculi network is visible within the lacunar wall.
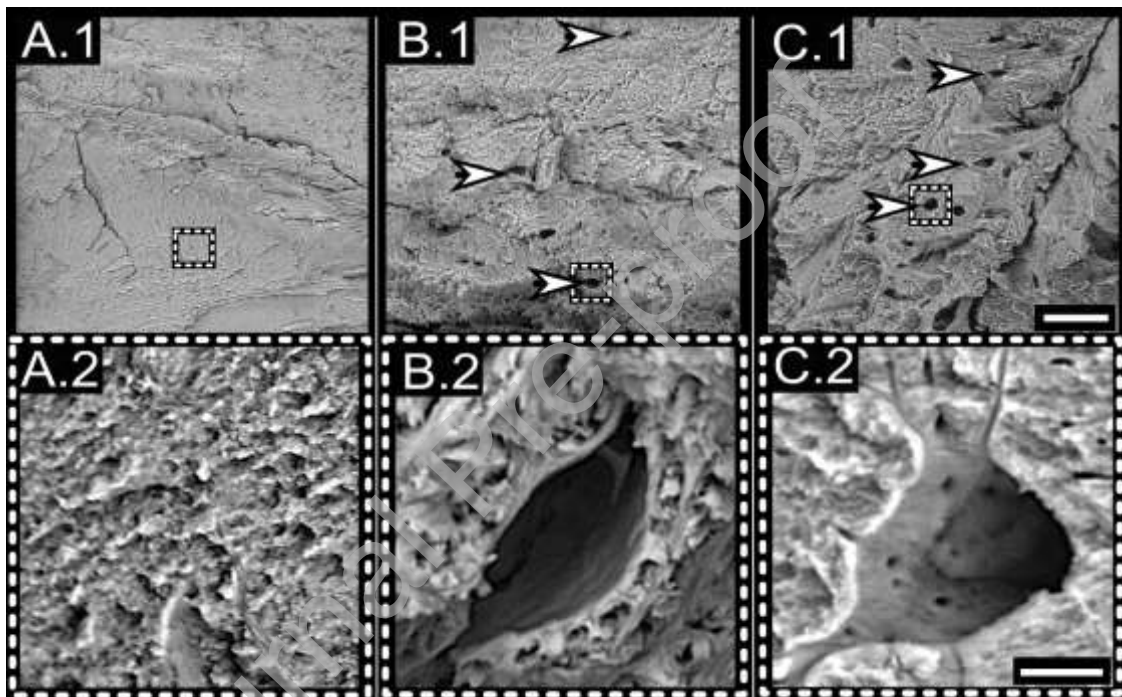

Figure 2: A comparison of structural differences between osteocytic and anosteocytic bones using scanning electron microscopy (SEM). (A.1) Anosteocytic pike bones rarely exhibit any cavities within the mineralized bone matrix, which is typical for such bones lacking osteocytes. **(A.2)** The enlarged image of anosteocytic pike bone, as indicated by the white dashed frame, shows a matrix of mineralized fibers. **(B.1)** The osteocytic cleithra of sturgeon exhibit visible osteocytic lacunae throughout the bone, as indicated by white arrowheads. **(B.2)** Close-up view of one osteocytic cavity, in which osteocyte cells reside in the living bone (enlarged inset within the white dashed rectangle). **(C.1)** Image of a fractured mouse femora reveals typical osteocytic cavities (indicated by white arrowheads). **(C.2)** Enlarged image of an exemplarily osteocytic lacuna (framed with dashed rectangles) in which canaliculi exit pores are visible in the lacuna wall. Scale bar in images on the top: 30 μm, Scale bar in close-up images on the bottom (white dashed rectangle): 3 μm.

3.2 An anisotropic matrix of fibrils and mineral nanoparticles

Mass density as determined by synchrotron-based absorption μCT imaging on different samples revealed that the bones have areas of higher (1.5 ± 0.3 g cm^{-3}) and lower (1.2 ± 0.4 g cm^{-3}) density. Measurements in a backscattered scanning electron microscopy (SEM) and

synchrotron based (XRD transmission) absorption measurements provided corroboratory estimates of average mass density values of 1.4 ± 0.4 g cm^{-3}, a value that falls within the variable range observed by the absorption µCT (see SI., *1.3.2 Determination of bone density* and SI Table 1). Thermogravimetric analysis (TGA) revealed a volatile liquid content of (10.3 ± 0.8) weight%, an organic component of about (26.8 ± 1.1) weight% with remaining ash content of $\sim(63.9 \pm 0.9)$ weight% mineral (mean values with STD, see also SI Table 2). Based on those findings we estimate that the mineral density for pike bones is 0.9 g cm^{-3}, similar to other fish bone, but with regions of local higher and lower density.

The material comprises mineralized collagen fibrils packed into layers that can be identified in orthogonal cc, dv and pd-planes (Fig. 3A). The 3D arrangement is well resolved with high-resolution synchrotron PCE-µCT, as shown for example in Figure 3B and SI Fig. 2. Layers of locally varying mineral density are easily discernable along the principal craniocaudal (CC) axis (highlighted in purple), with bright areas indicating higher density (enlarged image in Fig. 3C, and SI Fig. 3). The bones exhibit a transversal isotropic lamellar motif of the fibrous matrix. Orthogonal to the CC-axis channels run along the PD-axis and appear as pores visible in the PD plane. These channels are darker compared to the surrounding matrix and therefore depict a lower density. They, however, are not empty, as discussed below.
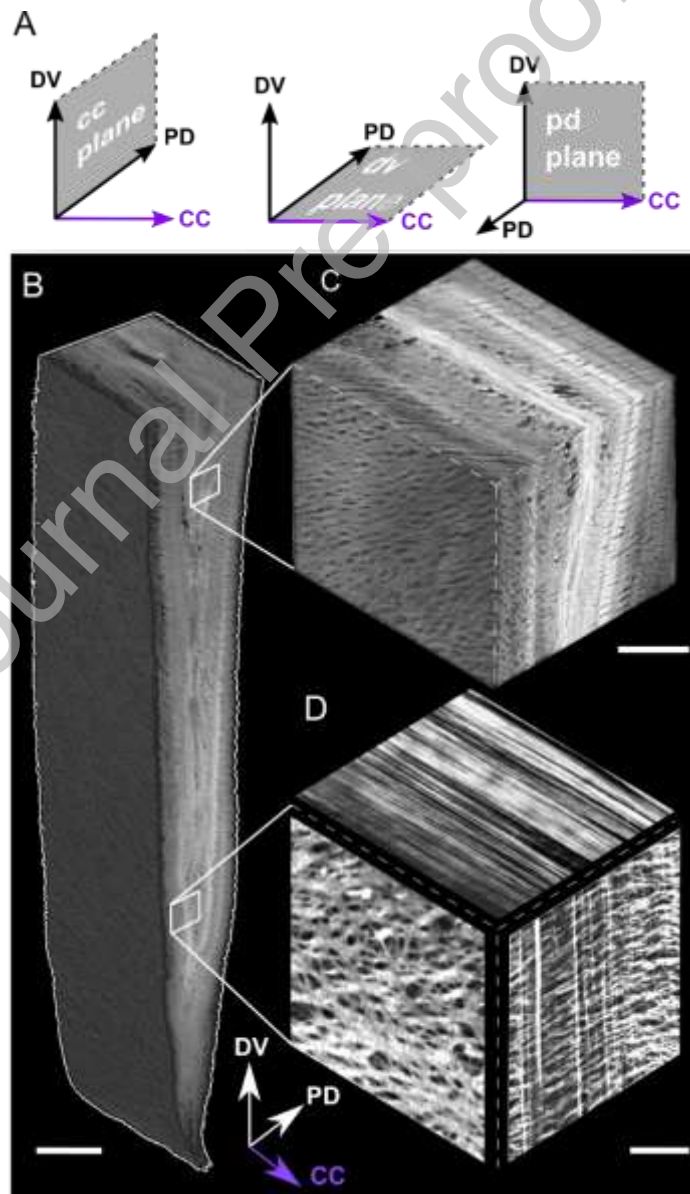
Figure 3: Three-dimensional (3D) arrangement of the mineralized collagen matrix: complementary contrasts of mineral and collagen. (A) Coordinate system used to describe the anatomical axes of the pike fish: craniocaudal (principal CC axis, highlighted in purple), dorsoventral (DV) and proximodistal (PD). The cc-plane corresponds to the surface spanned by DV x PD. The pd-plane corresponds to the surface orthogonal to the PD axes (DV×CC cross product). The dv-plane is spanned by the PD x CC axis. **(B)** High-resolution PCE-µCT [32] reveals alternating layers of lower and higher mineral density with orthogonal low density tracts. The intensity corresponds mainly to the local density, with minimal phase-contrast enhancement at edges. Scale bar: 50 µm. **(C)** Magnified region in the 3D PCE-µCT data exemplifies the juxtaposed higher and lower density domains in the mineralized collagen matrix. Scale bar: 10 µm. **(D)** Orthogonal views of similar bone segments produced by second harmonic generation (SHG) confocal laser scanning microscopy directly reveal the collagen fibrils. Three different structural motifs of collagen correspond to views in the three orthogonal anatomical directions of the bone. Along the principal axis (CC, highlighted purple), dense and compact parallel collagen layers (top view, dv-plane) appear to be pinned together by collagen fibrils oriented along the PD-axis (right-hand side of the quasi cube). Within the pd-plane (on the left-hand side), the pinning bundles appear dark. Scale bar: 10 µm.

The arrangement of collagen is directly revealed by second harmonic generation (SHG) images of fresh hydrated samples as shown for example in Figure 3D for the cc-, dv- and pd-planes corresponding to the CC, DV, and PD axes of the bone. The appearance of the collagen fibrils is very different when observed from the three orthogonal views with respect to the craniocaudal principal axis (Fig. 1). PCE-µCT and SHG images of various bones each reveal lower density fibrils in the cc-plane suggestive of less dense filaments running along the proximal distal (PD) axis, more or less orthogonal to the principal CC axis (see SI Fig. 4). These collagen fibrils likely pin the main pd-plane layers together. Fibrils running at various angles within the pd-plane layers contribute to density fluctuations visible in the dv-plane.

The collagen revealed by SHG appears to contain structural gaps which do not correspond to what is observed by PCE-µCT. The reason for this is that the SHG signal intensity depends on the relative orientation of both the incoming laser beam and fibril bundles. Out-of-plane collagen fibrils are not visible and only collagen fibrils in-plane excite sufficient signal to reveal the presence of collagen fibers. Complementary transmission polarized light microscopy (PLM) analysis confirms that the bone is densely packed with highly aligned collagen layers. The intensity of the demineralized bone is enhanced by Picrosirius red staining as seen by direct comparison between PLM and SHG of the same sample, shown in Figure 4A and B. Two relative polarization filter orientations are depicted with the (⊕ PLM) and (⊗ PLM) with magnified views given in Fig. 4A.2 and 4B.2, respectively. Identical regions in the three different figures are marked with (o) and (oo), for ease of comparison. The PLM analysis demonstrates that in fact the bone more or less uniformly comprises collagen fibril arrays, with few domains where the main fibril axis is not within dv-planes.
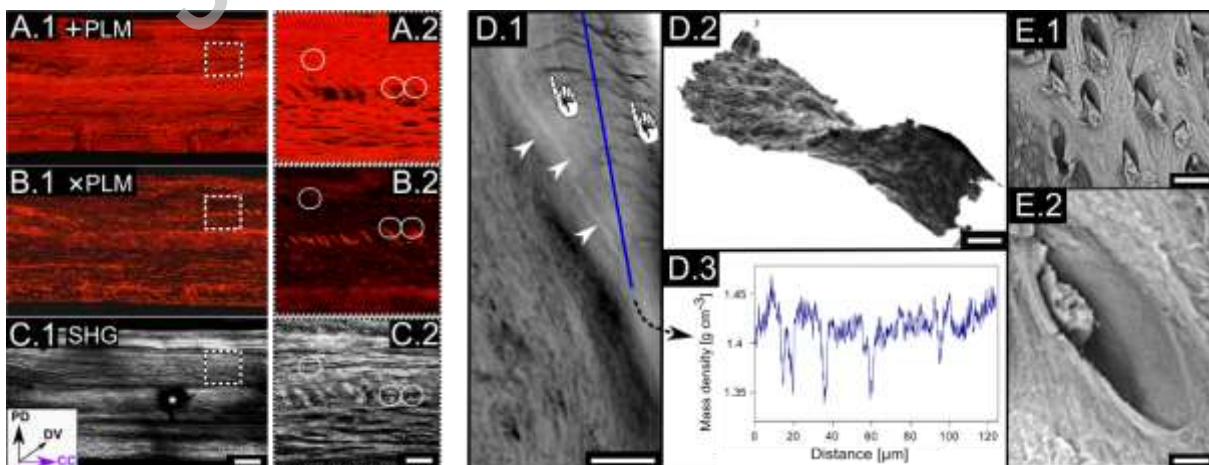
Figure 4: Microscopic organization of the matrix of anosteocytic cleithra. (A.1) Polarized light microscopy (PLM) images of demineralized and Picrosirius red-stained cleithra show collagen fibrils aligned mainly along the principal craniocaudal (CC) axis seen in the dorsoventral (dv-) plane (see Fig. 3). **(A.2)** Enlarged inset on the right-hand side shows magnified views of the main collagen orientation. **(B.1)** By rotating the polarization filters by 45°, off-axis collagen fibrils are revealed. **(B.2)** Enlarged image with off-axis fibril orientations as compared with image A. Compare identified spots (o) and collagen fibrils (oo). **(C.1)** SHG imaging of the same sample section reveals collagen fibrils, in plane, with fibrils oriented along both the CC- and the PD axis. Note an example typical SHG artefact due to an entrapped air bubble marked with an asterisk (*). **(C.2)** Enlarged SHG image depicts collagen fibrils in all orientations in the plane of the slice. Scale bars: 100 µm (inserts: 20 µm). **(D.1)** The nano-CT image of air-dried mineralized cut samples reveals local – micrometer length scale mass density fluctuations of the bone matrix. Dark wavy channels (pointers) of lower mass density are seen running across the main layers. Thin higher mass density layers (marked with white arrow heads) sandwich lower density layers. A profile along the bone demonstrates the local variations in density, as depicted by the blue line plot in D.3. Scale bar: 10 µm. **(D.2)** Enlarged 3D rendering of an example empty gap observed in the dehydrated bone near a low-density pinning channel due to shrinkage and separation from the background of the higher density layered bone matrix. Scale bar: 2 µm. **(D.3)** Line profile in a sample cross-section of nano-CT shown in D1, revealing typical fluctuations of the mass density. **(E.1)** SEM of the fracture surface of a wet-fractured sample shows the surface of anosteocytic pike bone that had been fractured when wet. The pores or channel entrances are filled with a fibrous material that resembles collagen fibrils. Scale bar: 10 µm. **(E.2)** Enlarged SEM image reveals a single pore containing a shriveled fibril. Scale bar: 2 µm.

Further insights into the fine structural arrangement emerge from nano-CT and scanning electron microscopy observations. A slice in the data (Fig. 4D.1) reveals juxtaposed thick, thin and very thin layers of variable density down to the sub-µm length scale. In different regions, parallel groups of filaments are seen (pointer in Fig. 4D.1), with orientations more or less orthogonal to the main structural layers (white arrowheads in Fig. 4D.1). The quantitative nano-CT data shows that the density of these filaments varies and in some regions appears to be extremely low, possibly indicating gaps in the structure, as shown by a 3D rendering of an empty space in the dry bone, shown in Fig. 4D.2. An example profile in the nano-CT 3D data (Fig. 4D.3) demonstrates approximately ± 10 % fluctuation in mass density across different layers. The very low-density gaps are presumably dehydration artefacts as they correspond to narrow irregular spaces located around the filaments inside the bone layers. These are demonstrated by SEM pictures of exposed pd-planes, shown in Fig. 4E.1 which correlate well with the pd-plane in Fig.3C and D. The low-density filaments appear to be separate from the layers of bone matrix, with these pinning fibers oriented orthogonal to the main layers. The pinning fibers in Fig. 4E.1 and E.2 relate to the pd-plane in Fig 3C and D and run along the PD-axis, visible in the cc-plane. The magnified Fig. 4E.2 suggests that when hydrated in the native tissue state, the filaments are thicker and presumably occupy the entire space (~4 x 15 µm) as they run along the PD axis. As opposed to hydrated bone, dehydrated fibers do not fill up the entire space of the channels, as these fibrils shrink (~3 x 5 µm) during dehydration.

3.3 A composite of locally varying chemical densities

The structure and density appear to vary locally on the micron length scale. Observed on cc-planes, the pike cleithra exhibits a very regular long range self-similarity of the biocomposite. This is seen by matching similar regions observed by nano-CT, SHG, backscattered SEM and energy dispersive X-ray spectroscopy (EDX). The nano-CT clearly reveals layering, with the main layers being pinned together with orthogonal, lower density filaments (Fig. 5A). SHG shows the nature of these filaments to be clusters of loosely packed, collagen fibril bundles (Fig. 5B). Backscattered SEM shows that the tissue has a rather uniform mineral density (Fig. 5C) although locally high and low density domains are visible. Comparisons with EDX measured on the same sample locations shows matching domains of calcium (Ca, Fig. 5D) and phosphorous (P, Fig. 5E) with inversely complementary domains rich in carbon (C, Fig. 5F).
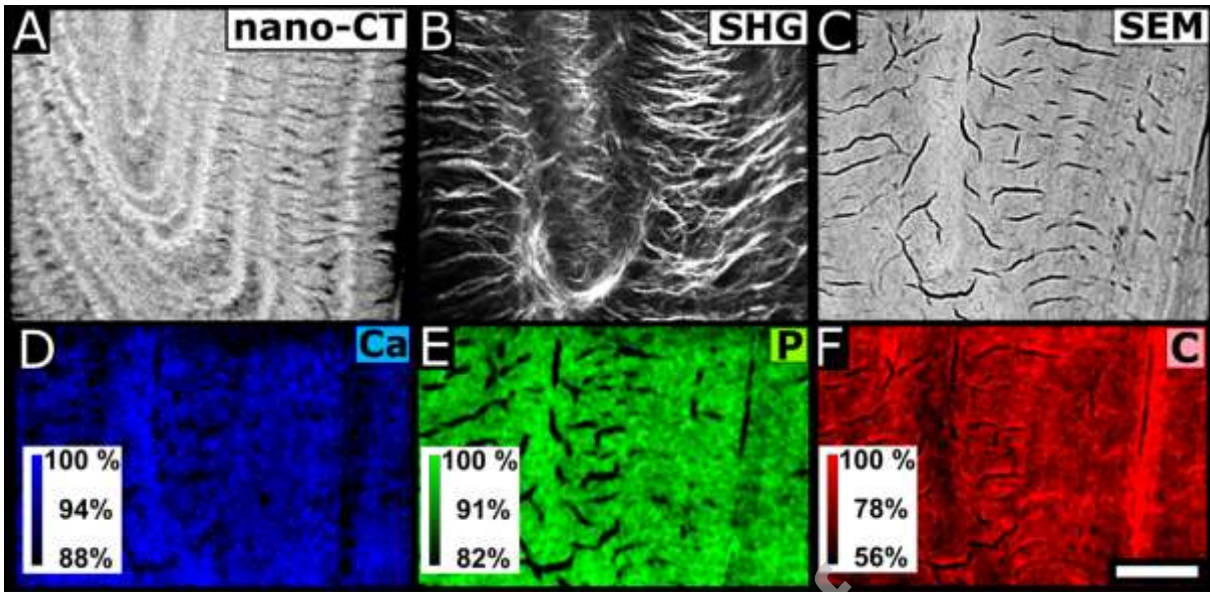
Figure 5: Density and mineral variations across layers on the micrometer length scale. (A) A nano-CT cross-section shows local fluctuations in the mass density distribution. Lower density tracts are seen orthogonal to the variable density layers. **(B)** SHG image reveals a complementary view of the curved and wavy arrangement of cross-layer collagen fibrils. **(C)** The same sample imaged by SEM shows the surface of a cut and polished sample. The backscatter electrons disclose layers of low and high mineral density as well as orthogonal low-density tracts. **(D)** 2D EDX maps of the same area show complementary Calcium (Ca) distribution in blue, **(E)** the phosphorous (P) distribution in green, and **(F)** the carbon (C) distribution in red. Scale bar: 50 μm.

3.4 Mechanical correlation with anatomical anisotropy

The elongated arrangement of mineralized collagen fiber layers suggests that these bones should have anisotropic properties. Analysis using complementary mechanical-testing methods was thus performed on hydrated cleithrum samples cut along all three CC, DV and PD anatomical axes (Fig. 6A.1), applied to cubes or elongated beam samples (Fig. 6A.2). The sample preparation and mounting allow direct comparison between the results of three-point bending, micro-indentation, and compression tests (Figure 6B).

All the experiments show that the Young's modulus is ca. x2 higher along the primary-craniocaudal (CC) axis, as depicted in Fig. 6C. Along this orientation, moduli values derived as approximations based on HV indentation tests are somewhat lower than those obtained by compression or three-point bending tests, averaging at 5.7 versus 9.3 and 10 GPa, respectively. Vickers hardness (HV) values (median ± standard errors) are transformed into estimations of Young's moduli by using SI eq. (6) as summarized in SI Table 3. It is possible that the relationship between indentation and moduli is not as similar to observations in other bones, though we believe that indentation underestimates the bone stiffness when applying load orthogonal to the cc-planes, possibly due to splitting between layers along the primary collagen fibril CC layers. The values for the two orthogonal anatomical axes (DV and PD) span 3-4 GPa and are similar though statistically significantly different from the CC axis. The results plotted in Fig. 6C are summarized in Table 1 (see also SI Table 3). Note that it was not possible to measure the samples in bending in the PD orientation due to the thin aspect ratio of the bones.
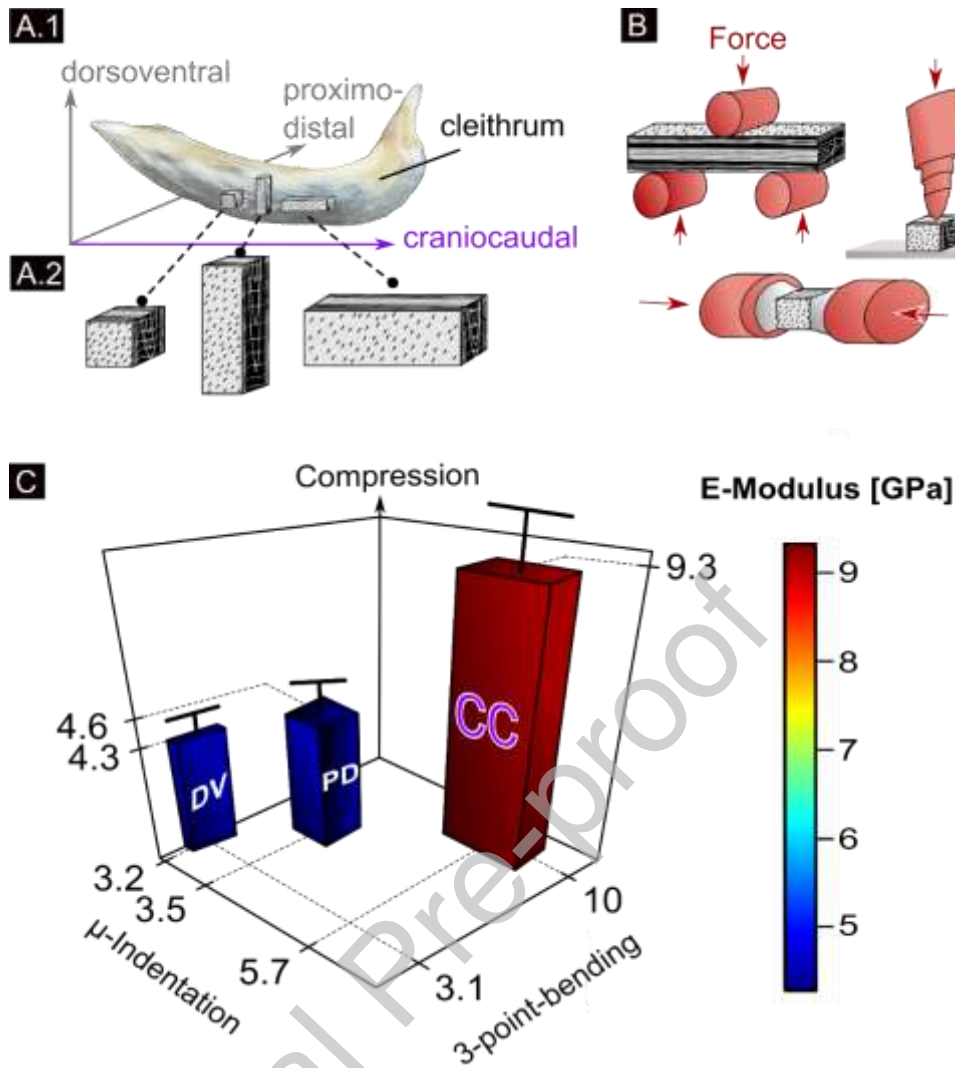
Figure 6: Mechanical properties of cleithrum bones by three-point bending, µ-indentation, and compression tests. (A.1) A photograph of a cleithrum bone sample and **(A.2)** a schematic of the extracted samples, showing three anatomical axis directions of the pike fish: craniocaudal (CC), proximodistal (PD), and dorsoventral (DV). The craniocaudal direction, indicated by purple highlighting, is the principal orientation axis. Mechanical testing was performed using cubes and beams, as identified by the black dashed lines. **(B)** Different (untested) samples were subjected to three different types of measurements: 3-point bending tests (upper left), µ-indentation (upper right), and compression testing (bottom) with strain analysis performed contactless, by DIC. **(C)** 3D presentation of the results of measurements of Young's moduli of the cleithrum bone in relation to anatomical orientation and mechanical testing method.

Measurement-direction	E-modulus [GPa]					
	µ-Indent.	**n****	**Compression**	**n**	**3-point bending**	**n**
CC	5.7 ± 1.3	4	9.33 ± 0.58	20	10.0 ± 3.0	18
DV	3.2 ± 0.5	4	4.29 ± 0.31	30	3.1 ± 1.3	10
PD	3.5 ± 0.7	4	4.57 ± 0.18	70	---	

Table 1: **E-Modulus in pike fish cleithra for three anatomical directions.** Median values and standard errors for the dorsoventral (DV), craniocaudal (CC), and proximodistal (PD) anatomical directions were obtained from micro-indentation (µ-Indent.), compression testing, and 3-point bending experiments. The number of samples tested for each method is denoted as n. In the µ-indentation experiments, for every tested fish (n**=4), a total number of 30 indents were applied, yielding HV values that were converted into approximations of Young's modulus according to [46,47], see SI Table 3.

3.5 Nanocrystals as strain sensors and indicators of residual stress

XRD analysis was used to reveal cAP crystal deformation along the main CC bone orientation, across the dv-plane. For every point, exposure times were limited to a few seconds to minimize radiation damage to the collagen [39]. Diffraction pattern measurements yield either complete- or partial (002)-Debye rings (depending on the degree of fibrillar order) produced by the apatite nanocrystals (Figs. 7A.1 and A.2, bright arrows point to partial rings). The patterns observed when X-rays propagate along the DV axis orthogonal to the dv-plane (see Fig. 7.A.2) reveal bright, well-defined partial arcs. They appear due to a rather highly textured arrangement of mineralized fibrils in the plane, corresponding to the fibrous layered arrangement revealed by the other imaging methods. When X-rays propagate along the CC axis scanning across the cc-plane (see Fig 7.A.1), a powder-like but low-intensity full-ring is observed suggesting no preferred texture in the cc-plane and an overall weaker cAP signal. When analyzed in this orientation, the mineralized collagen fibrils appear poorly oriented and the diffraction signal is weak because the majority of fibrils and the c-lattice of the crystals are aligned along the X-ray beam path that does not reveal the (002) ring. When examining results across the thin proximodistal (PD) direction, the c-lattice parameters of the cAP nanocrystals increase towards larger d-spacings in the central bone regions, as compared to measurements on the proximal and distal sample surfaces. Example results for one bone sample, measured across the dv-plane, along the proximodistal axis (corresponding to the scans described in Fig. 7 A.2), both fully hydrated as well as following dehydration, are shown in Fig. 7.B. The average and standard deviation of similarly measured d-spacings in 3 hydrated bones from 3 different fish are compared in the center and outer regions in SI Fig. 5, revealing c-lattice constants spanning 6.865~6.878 Å. When comparing each sample with measurements performed after dehydration, the cAP nanocrystals on the proximal and distal aspects are more compressed, becoming ~0.13 % shorter, likely due to the stress induced by the shrinking collagen fibrils that are tightly attached to the cAP nanocrystals. Comparison between the outer-surfaces versus and central cAP crystal lattice parameters between the proximal and distal aspects of the bone reveals a ~0.15 % difference (SI Fig. 5), suggestive of compression residual stresses along the CC axis of these bones. Three additional samples measured first dry, and then following 1 hour annealing at 260 °C to denaturate the collagen fibrils (data not shown), revealed 0.14 ± 0.02 % and 0.09 ± 0.02 % strains due to collagen destruction.

We used synchrotron-based diffraction-orientation micro-computed tomography (XRDo-μCT) to obtain a quantitative measure of the orientation anisotropy of the cAP mineral crystals, with respect to the principal craniocaudal axis. The average arc intensities along and orthogonal to the CC axis (on-principal-axis and off-principal-axis, respectively in the dv-plane), collected from XRDo-μCT measurements obtained by repeatedly scanning and rotating samples 180° around the CC axis, create sinograms of intensity per lateral position versus rotation angle. These were used to produce ("reconstruct") cross-sectional mean diffracted intensity maps of the (002) peak. Figure 7C shows 2 such reconstructed XRDo-μCT cross-sections. The PD axis is marked for orientation (see white arrows). Comparisons of the on-principal-axis (Fig. 7C.1) and off-principal-axis (Fig. 7C.2) intensity distributions highlight the much larger population of crystals lying along the principal CC bone axis, as compared to the orthogonal DV and proximodistal (PD) orientations. The ratio of on-principal-axis to off-principal-axis intensities for each sample point provides an indication of the degree of the anisotropic arrangement of mineralized collagen fibrils at each XRD point as seen from each sample rotation angle. A histogram shows that in most bone regions, the average (002) intensity is ~5-15 times stronger along the principal CC axis, peaking at a ratio of 7. Absorption reconstruction of the transmission measurements corresponding to the XRDo-μCT maps shows that at the rather low 25 μm resolution of these scans, pike bones exhibit rather homogeneous absorption (as shown in Fig. 7C.4) with somewhat lower densities encountered on the outer (proximal and distal) bone surfaces. Corresponding XRF-μCT

16

reconstructions of the same bones reveal chemical maps in which somewhat higher concentrations of zinc (Zn) are found in the same lower-density outer sample surfaces (Fig. 7C.5). Lab-based XRF maps confirm the same trend of elementary distribution of Zn as provided in SI Fig. 6 and quantitative elemental content in wt% of the pike bone can be found in SI Table 4. This is different from strontium (Sr, Fig. 7C.6) that is present at low counts with more or less the same distribution, presumably uniformly substituting a small percentage of the Ca in lattice locations of the cAP. The XRF sum spectra of all measurement points (shown as the blue curve in Fig. 7D) reveal the presence of Zn and Sr. However, these elements are very dilute, corresponding to an average of 0.03 wt% and 0.02 wt% respectively, as determined by ppm-sensitive quantitative X-ray fluorescence spectrometry (SI Fig. 6, 7 and SI Table 4). This may explain why they were not detected using conventional energy dispersive X-ray (EDX) measurements of the same samples (compare red and blue curve in Fig. 7D, corresponding to the EDX and XRF sum spectra, respectively).
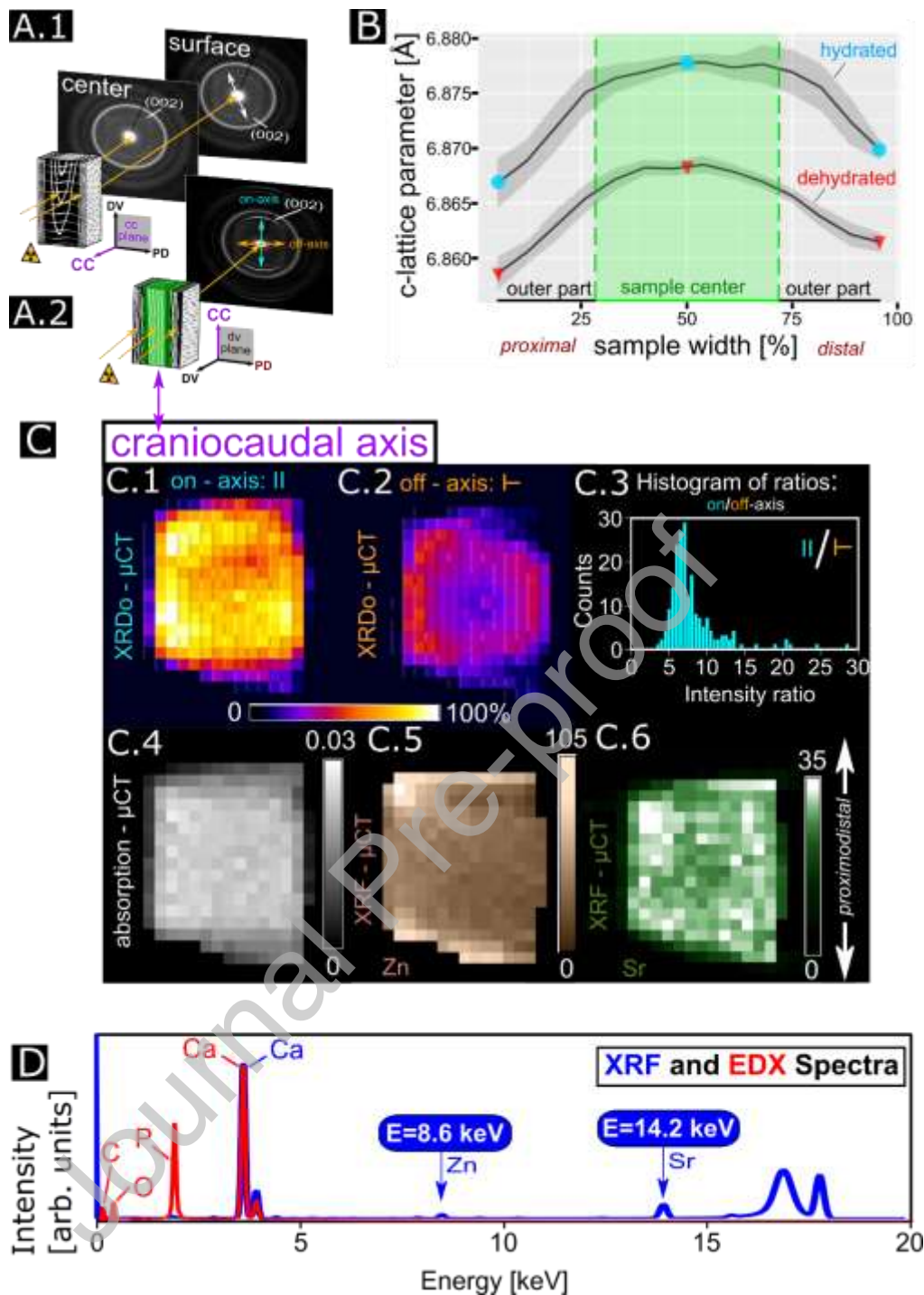
Figure 7: Nanocrystal lattice parameter, preferred orientation and relation to Zn and Sr elements in the composite comprising cleithra bones. (A.1) Schematic of X-ray diffraction (XRD) measurements illustrates an X-ray beam (yellow arrows) irradiating the cc-plane and X-rays are propagating along the CC-axis. Along the cross-sectional sample, the texture changes from the outer regions revealing randomly dispersed mineral crystals in the center of the sample. **(A.2)** The X-ray beam (yellow arrows) illuminates the dv-plane (Fig. 6A.2, sample on the right) and X-rays are propagating along the DV-axis, revealing the highly oriented collagen fibrils. **(B)** Averages of the c-lattice parameters and the standard deviation (highlighted in light gray) of cAP is shown for one representative pike bone sample, as determined along the bone cross-section, from proximal to distal (PD), corresponding to the scans described in A.2. The same sample was measured hydrated (marked in blue) and dehydrated (marked in red) across the cleithrum width at different positions along the CC axis. Areas close to the outer sample surfaces are the outer (proximal, distal) parts, and the sample center is highlighted in green. An average of the outer and central c-lattice parameters of three

different cleithra are shown in Supplementary Figure 5. **(C.1)** X-ray diffraction-orientation micro-Computed Tomography (XRDo-μCT) reconstruction of the on-principal-axis intensity of the (002)-Debye rings of mineral nanoparticles. The intensity distribution is somewhat lower in the center, showing that many crystals are oriented parallel to the craniocaudal bone axis (on-axis). **(C.2)** Average X-ray arc intensities orthogonal to the CC axis (off-axis in the dv-plane) with most regions exhibiting ~2-5x lower intensity corresponding to fewer cAP crystals in this orientation. **(C.3)** A histogram of the anisotropy intensity ratios between on-/off-axis for all measured points. Similar distributions are seen for other slices. **(C.4)** Absorption-μCT of the same cross-section. Higher absorption is indicated by brighter regions in the reconstructed slice. Lower absorption is seen on the proximal and distal bone sides. **(C.5)** XRF-μCT shows elemental distribution of zinc (Zn) within the cross-section of the cleithrum, with higher counts observed on the proximal and distal surfaces. **(C.6)** XRF-μCT reconstruction of strontium (Sr) reveals a distribution of low counts within the sample cross-section. **(D)** XRF sum spectra (blue curve) show peaks corresponding to Zn and Sr. EDX sum spectra of the same sample (red curve) could not detect those trace elements.

3.6 Fibril orientations and hydration modulate strength and fracture behavior

Bending and fracture experiments provide insights into how the bone layout contributes to the long-term performance of the whole structure. Three-point bending tests of samples, in which both tensile and compression stresses act, demonstrated that orthogonal to the CC principal bone axis, the wet bones are rather weak, yielding at below 40 MPa. This is low as compared with other bones, e.g. mammalian cortical bone, for which yield strengths of 80-150 MPa were reported in tension, as compared with 130-220 MPa reported in compression [48,49]. Curiously, however, the fish cleithrum samples do not fracture when measured wet, only when tested dry, in which case the yield strength becomes impressively high, exceeding 180 MPa. Figure 8A demonstrates the three-point bending experiment performed. Average stress-strain results for n=28 wet samples are shown by the blue curve in Fig. 8B with several dry bone samples (n=3) shown for comparison (Fig. 8C). The arrowhead identifies the point where the deformation stops being linear, which we identify as a yield point, for comparison between the wet and dry cleithrum samples. Note, however, that during three-point bending, the wet samples never fail catastrophically, rather they continue to carry load as failure accumulates. Undulations are observed at different extents of excessive deformation, as seen for different samples (SI Figure 8) indicative of repeated, gradual rupture. Indeed, SEM images of the fracture surfaces show huge differences in the appearance of the broken segments where the wet samples resemble greenstick bone fractures (SI Fig. 9). Higher magnifications of the fracture surfaces show vastly different textures in the wet versus dry states: extensive fiber pullout and unravelling is seen in the wet case (Fig. 8D and SI Fig. 9) whereas brittle shattering is seen in the dry, non-physiologic case (Fig. 8E). Note that due to limitations of our experiments, only low strain rates of 0.02~0.03 % s^{-1} were conducted, and that mainly wet samples were tested, since the dry samples do not represent the normal conditions under which the cleithra bones operate *in vivo*.
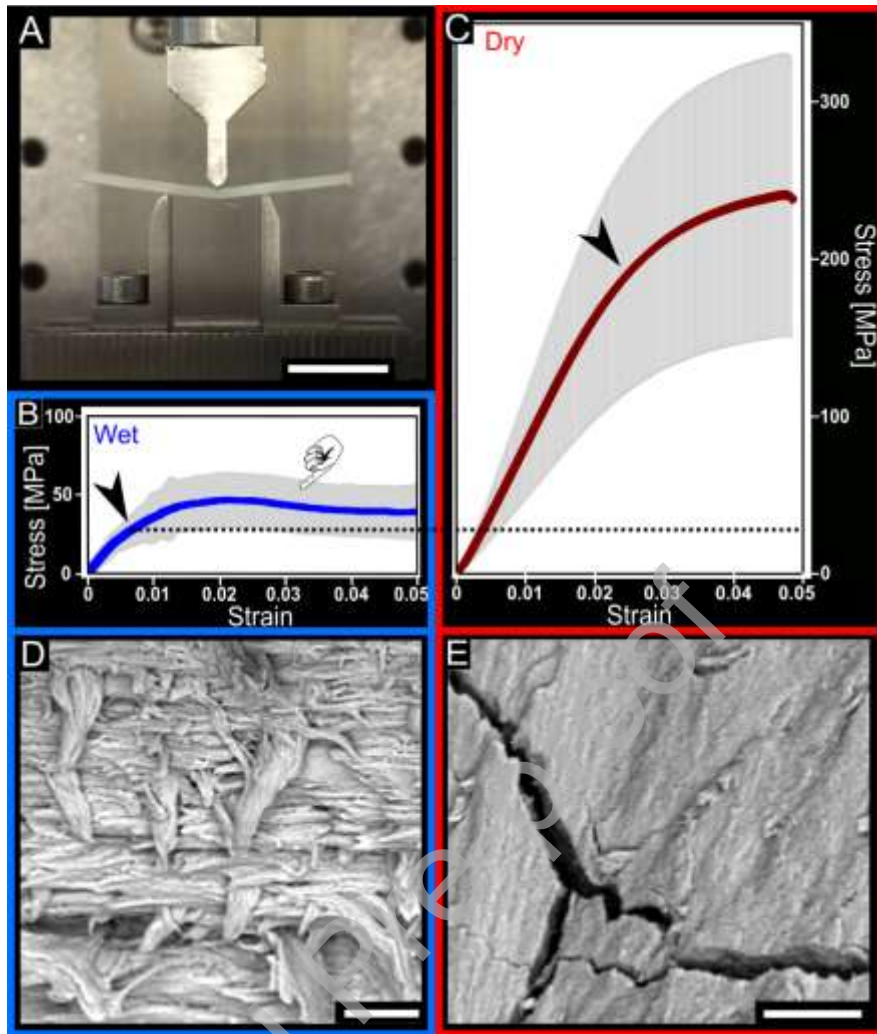
Figure 8: Comparison of mechanical strength tests in dry and wet pike bones show brittle versus tough behaviors. (A) Three-point bending experiments performed on bar-shaped samples reveal vastly different strength and yield behavior. Scale bar: 1 cm. Blue frames denote wet samples, and red frames dry ones. In this experiment, only the principal CC axes of all samples were tested in wet and dry conditions. **(B)** Bending experiments performed on fully hydrated cleithrum samples (n=28) show yield around 30~50 MPa with an extended post-yield stress-strain curve (blue). The standard deviation of the averaged curves is depicted in light grey. The black arrowhead in the graph indicates an average yield point. After reaching the maximum the load carrying capacity decreases with an inflection point observed in the wet samples (finger pointer), indicative of additional fibers in deeper layers carrying load, leading to an extended post-yield region. It should be noted that many samples did not experience failure even at the highest displacements possible on the testing equipment. **(C)** Dry samples exhibit 3x~5x higher strength and brittle failure as demonstrated by an average stress-strain curve (red) of bending tests on dehydrated cleithra (n=3, standard deviation represented by the gray zone). The arrowhead points to the yield position, where the linear response to stress ends. Compare the yield with the dotted line indicating the much lower yield point of hydrated samples. **(D)** SEM images reveal the ripped-out fibers and fibrous appearance of the fracture surface of a wet-fractured sample (low magnification view is shown in Supplementary Figure 9). Scale bar: 10 µm. **(E)** SEM image reveals the brittle fracture appearance of a surface of a dehydrated cleithrum bar-shaped sample. The surface appears relatively flat and homogeneous and shows multiple fast-propagating cracks. Scale bar: 10 µm. The wet and dry experiments were conducted using different three-point bending machines as described in the Materials and Methods section.

20

4. Discussion

The double-curved cleithrum bone appears to be well designed to sustain repeated tensile loading. This is presumably important for long term (years) of rapid gaping, a function that is essential for the pike ambush hunting habits. These bones are light-weight, low density and resist rupture though they are very thin. They have a wing-shape that is macroscopically and microscopically very different from the bones found in mammals. Though of unremarkable absolute strength, cleithra do not fracture catastrophically, which is presumably good for survival. The average mechanical properties are similar to what has been shown for a range of other fish bones [25]. The highly anisotropic layered texture, with locally varying densities and cross-layer pinning fibers, appear to produce a pre-stressed damage resistant composite structure, where in-plane compressive residual strains are localized to the outer (proximal and distal) surfaces. Though we cannot rule out some gradients in compositional variation due to e.g. minute amounts of Zn incorporation, the strong deformation response during dehydration suggest that evolution makes use of the tight coupling between collagen and cAP crystals to enhance the strength of these. The cleithra bones may therefore be interesting bio-inspiring models for smart nanocomposites.

Our findings of higher c-lattice distortions in the cAP nanocrystals of the proximal and distal surfaces of these bones suggest that nature makes use of residual compressive stresses in a manner that is similar to high performance engineering materials. Industrial examples include reinforced concrete in which a stiff matrix surrounds tension pre-stressed steel wires [50,51] or tempered glass structures, where the outer surfaces are compressed with respect to the inner layers following rapid cooling [52]. Cleithra show how evolution has long known about these concepts and has implemented them on the nanoscale of fish bones for improving the mechanical properties of light-weight repeatedly loaded structures. X-ray diffraction mapping revealed gradients in the cAP c-lattice parameters between the center and outer bone surface. These have the same magnitude as strains induced by dehydration. It has recently been proposed that during bone formation, collagen fibrils contract due to intrafibrillar mineralization, which can result in creation of stresses of a few MPa [53]. Our measurements in the outer bone regions of cleithra (~0.15 %) suggest that the cAP crystals experience high compressive stresses reaching ~150 MPa along the bone axis. This presumably acts against any instantaneous muscle loads and asymmetric bending moments. We hypothesize that compression stresses on the outer layers may hinder damage formation by preventing cracks from entering the structure whereas alternating densities and wavy fibers work against crack propagation across the structure [2].

Our data suggest that the cleithrum bone is well designed to function in a manner comparable to a coupling rod (con-rod) found in combustion and steam engines, connecting the driving wheels to the power source operating cyclically in tension and compression [54]. The thin and flat structure of the cleithrum allows for low friction rapid movement along the fish body axis during repeated jaw activation events while employing the gape-and-suck feeding that is used by the pike during hunting [27,28]. Naturally, the cleithra must not bend or buckle, but rather elastically transmit the stresses applied, while resisting fracture or rupture, to ensure that the fish survives.

One possible way to accomplish resistance to shear forces and buckling is through the arrangement of the dense and interconnected mesh. Adjacent collagen lamellae are "pinned" together with wavy collagen fibers, not unlike the low-density fibers shown for another acellular bone, tilapia [55]. Similar to those observations, the pinning collagen fibers in pike cleithra are hypo-mineralized and are oriented perpendicular to the principal lamellae providing low stiffness and high toughness. Those fibers create canal structures that could under certain conditions, amplify stresses and strains [3]. However, a mismatch in stiffness between the canals in which the pinning fibers reside within the surrounding matrix, may lead to redistribution of excessive strain energy during loading and therefore may help prevent

cracks from forming averting stress concentrators [56]. This directly contributes to crack deflection and increasing toughness of the bone material [12]. Such a mechanism has been proposed to help strengthen teeth, where accumulation of small cracks prevents complete failure and hinders crack propagation under load [57].

The cleithrum bones function as complete structures as part of the pectoral girdle, critical for food ingestion by the fish. The structural and strain gradients that we observe presumably help the bones cope with the stresses they are exposed to, reducing the need for remodeling. The lack of osteocytes in these bones raises the possibility that – unlike mammalian bones - they are not able to remodel, and possibly they do not need to do so during the lifetime of the fish. We noted that extracting and cutting-out segments of bone for testing, by removing parts from the highly-anisotropic samples always yielded compromised mechanical performance. These results suggest that, similar to other composite structures, the whole intact bone outperforms cut-out segments. Wet bone cubes and beams exhibited a yielding strength of only ~40 MPa, with gradual, although partial, rupture. Impressively, during three-point bending experiments in beams cut from these bones, most samples did not reach complete failure (Supplementary Figure 8). Similar large deformation behavior was reported in other fish bones [25,55]. It is likely that the extensive failure resistance is enhanced by the low mineral density, which for our pike samples is similar to the anosteocytic tilapia opercula, where a mineral density of ~0.9 g cm^{-3} was shown. Curiously, osteocytic fish bones also have low mineral density (reported e.g. for carp to be ~10 % lower than pike [25,55,58]). The lower density of fish bones, as compared to mammalian bones (1.2-1.6 g cm^{-3} [55,59,60]) is, therefore, likely not related to the presence or lack of osteocytes. It is not clear if there is a connection between osteocyte remodeling [61] and bone density, though clearly mineral removal or deposition should play some unknown role in this regard. We speculate that in fish, perilacunar interactions are less involved in affecting the mineral density of the cleithra.

The high toughness and crack prevention design and cAP nanocrystal pre-stress gradients presumably help these bones resist catastrophic failure, which is essential for bones lacking osteocytes that may not be able to heal. The fact that pike cleithra bones continue to sustain loads far beyond yield may be linked to the presence of orthogonal (cross-ply) crimped fibrils, that become loaded when surrounding layers rupture or fail during overloading, as evidenced by the inflection seen in the 3-point bending curves (finger pointer in Fig: 8B) when the bones are loaded beyond the yield point. Impressively, following dehydration, cleithra become ~5x stronger. Additional measurements of stiffness performed on dry samples (data not shown) demonstrated that some bones reach a bending Young's-modulus of 20-30 GPa. The post-yield region of such dry bones is small due to brittle fracture. This marked shift in both yield and post-yield behavior can be attributed to the appearance of high compressive residual stresses on the outer bone regions following dehydration. It is noteworthy that dehydrating the fish bones can be compared to shifting the material upwards in an Ashby plot of strength versus density. The dehydrated bone exhibits properties comparable to tendons. It is possible that the cleithra should be compared to mineralized tendons, such as the mineralized turkey leg tendons containing unidirectional collagen fibers, where a mass density of 1.6 g cm^{-3} [62,63] has been reported (which is similar to the mass density of the pike bones). Function is similar in the tendons and in the cleithrum, as both are repeatedly and cyclically loaded in both tension and compression along the long axis [64]. Previous studies have demonstrated how the mechanical properties of tendons are influenced by the strain rate [65]. Studies on Achilles tendon (applied strain rates: 1 and 10 % s^{-1}) [66] as well as human- and horse tendons (applied strain rates: 0.3 and 0.6% s^{-1}) [67] showed an increase in strength with increasing strain rate which we were not able to reproduce in our pike cleithra. We speculate, however, that the cleithra may have a dynamic strength whereby, similar to tendon, the bone becomes stronger at higher loading rates. An interesting possibility is the likely capacity of the structure to elastically deform and therefore to store energy. Indeed, it has been shown in turkey tendons that the maximum strain

22

reported is ~10 % [68], while bones in teleost fish, such as the North Atlantic herring, have a greater ability for tensile deformation (~up to 20%) [69]. When the cleithrum bone is loaded in tension during mouth opening, the energy generated may cause the fibers to stretch, similar to the way mineralized tendons in avian stretch during locomotion [70]. The bones may thus store elastic energy during rapid gaping, to help in swift, energetically efficient mouth closure. Further studies are needed to test this, as, due to limitations in the present study, it was not possible to change the strain rates (0.02~0.03 % s^{-1}) within our experiments.

The compressive residual stresses observed near the outer bone surfaces, do not correlate with regions of increased zinc content and lower mineral density of the cleithrum bone (see Fig 7C.5 and SI Fig. 6C.1 and C.2). Whereas zinc can in principle alter the cAP lattice parameter [71], it is not clear if it does in the fish bones. On the other hand, it is a biologically essential component of matrix metalloproteases with important cellular functions. Quantitative measurements show no correlation between alterations in Zn content and reduction in c-lattice parameters in pike bone, as demonstrated in SI Fig. 10. Compared to studies where c-lattice parameters are reduced due to Zn content [72], there is too little Zn within the pike bone (SI Table 4) so that Zn doping of the crystals can be more or less excluded. It is likely that the outer bone surfaces have a higher organic content and are therefore less dense and contain more Zn in the organic tissue. Increased organics suggest that there should be greater amounts of biologically active zinc (e.g. metalloproteases). Indeed, Zn concentrations in previous fluorescence studies did not find clear correlations between mineralization and Zn levels in human bone tissue [73].

While our results suggest that zinc is likely not enriched within the cAP crystal lattice as a substitution, the situation is different for strontium. Sr is present in low concentrations in the mineral of bone [73] distributed relatively homogeneously within the matrix, as our XRF-µCT results show (Fig. 7). Both Zn and Sr can be detected in these bones with XRF methods however due to the low concentration (very low counts, in a range of a few ppm), they are not detected by the less sensitive methods of EDX.

The collagen fiber mesh of the cleithrum is devoid of bony lacunae containing osteocytes, which is different from mammalian bones. The fish bones are free of these stress raisers, and therefore they have fewer internal defects which reduces the chances of crack initiation. The bone also has a relatively low mass with a bone mineral density that is less than 1 g cm^{-3} (see Fig. 3 and SI Fig. 3 for an example of regional variations in the density). In many skeletons the solution to increase strength is by increasing material mass or creating larger geometries. In the pike however, a major source of increasing strength seems to arise from introduction of residual compressive stresses on the larger outer proximal and distal surfaces. Usually, bones less capable of repair (for example the skull) are engineered with a higher safety factor (The skull bone is estimated to have a factor of 40 whereas the tibia has a factor of 4 [7,74]). We therefore hypothesis that the cleithrum is excellently adapted to withstand cyclic loading in tension and compression and achieves sufficient strength by lacking internal osteocytic porosities as well as strengthening by layering and compressive strains on the outer surface.

Transversal isotropic mechanical properties, as revealed by three-point bending, compression, and µ-indentation experiments, identify the CC axis to be the strongest, aligned with the long bone axis and the orientation of forces. Due to anatomical limitations and the thin dimensions of the bone, conducting 3-point bending tests along the proximodistal axis was not feasible. Young's-modulus values of teleost fish have been reported to vary between 5 and 8 GPa [55,58,75], while our findings show a range of 3 to 10 GPa, depending on the anatomical orientation, and indicating that wet pike bone is less stiff but tougher than mammalian bone. Mammalian cortical bone in the axial orientation of the long bones is reported to be in the range of 15~25 GPa [6,55]. Our results match other observations in the anosteocytic bone of tilapia, where Young's modulus of E = 6.1 ± 2.7 GPa was reported [55].

Compared to 3-point bending and compression tests, estimates of Young's-modulus based on transformation of HV values of µ-indentation tests are lower. It is possible that unlike other bones, the conversion of HV into Young's modulus, eq. (6) found in the SI, does not work well for such low-density bones. Yet an alternative reason for this might simply be splitting of collagen fibers during indentation along the CC axis. Previous work has suggested that anosteocytic bone exhibits highly dynamic water permeability [76]. Small gaps between mineralized collagen fibers allow for solvent permeation in pike bones [77]. Our work finds that as the bones dehydrate, they become much stronger. During dehydration, the collagen fibers within the dense bone matrix shrink, leading to mineral compression by ~0.13%. This is similar to dentin [78] and is on the same order as previously reported for canine fibulae [79,80]. This is possible because laminated layers are composed of mineral nanoparticles attached to highly oriented collagen fibrils, primarily along the principal craniocaudal axis in cleithra. The alignment of collagen fibrils has been studied using various methods [81–83]. Since water removal causes collagen to shrink and apply stresses into the mineral, water content may have a direct influence on modulating strength of the cleithrum bones. We note that it has been reported that dehydration increases the elastic modulus, as has been observed previously in third metacarpal PMMA-embedded mammalian bones, as determined by nano-indentation experiments [84]. Further work is needed to assess the role of water modulation and effects of increasing the strength of these bones.

This work demonstrates a direct link between interactions on the nanoscale and the mechanical performance of the anosteocytic cleithrum bone in pike fishes. Cleithra are composites of bone ingredients, mainly mineral, collagen, but where water may also play a mechanical role. Our analysis shed light on fundamental design principles with variable properties of the cleithrum depending on composition and geometry. From a mechanical perspective, the structure benefits from the lack of osteocyte cells. Our results suggest that cleithra exhibit a high degree of flexible strength, tunable by water content on the nanoscale, which generates a design well adapted to be repeatedly loaded, yet prevent rather than heal damage.

5. Conclusion

The structural- and mechanical functional relations of pike bones are evolutionarily designed to prevent damage, repeatedly loaded rapidly. Our study, using various low- and high-resolution imaging and mechanical testing techniques, showed that although the thin anosteocytic pike fish cleithra bones have similar components to those found in other vertebrate bones, they merge compressive residual strains on the outer surfaces, with micrometer scale fluctuation in density, while minimizing internal stress raisers due to a lack of osteocytes. The composite structure is lamellated, compact with a transverse-isotropic appearance and clearly anisotropic mechanical properties. A principal collagen orientation contributes to higher Young's moduli along the caudiocranical (CC) axis, more than double the values found along the two other perpendicular anatomical orientations. Removal of water increases the bone strength ~5x completely changing the appearance of the fracture surfaces. When the bones are dehydrated, collagen fibers act to compress the apatite nanocrystals and the observed strain of ~0.13% suggests that the collagen and mineral are bound tightly, sustaining stresses exceeding 180 MPa. But the wet bones exhibit gradients in nanocrystal deformation and strain from the center outwards. The cAP nanocrystals appear to be preloaded near the bone outer surfaces (proximal, distal) by ~0.15% presumably contributing to resistance to crack initiation. These features make the cleithra well designed to sustain rapid loading cycles required by the pikes for rapid gape-and-suck swallowing of prey.

Data availability

The data that support the findings of this study are available from the corresponding author upon reasonable request.

Declaration of Competing Interest

The authors declare that they have no known competing financial interests or personal relationships that could have appeared to influence the work reported in this paper.

References

[1]   M.A. Meyers, J. McKittrick, P.-Y. Chen, Structural Biological Materials: Critical Mechanics-Materials Connections, Science 339 (2013) 773–779. https://doi.org/10.1126/science.1220854.

[2]   O. Kolednik, J. Predan, F.D. Fischer, P. Fratzl, Improvements of strength and fracture resistance by spatial material property variations, Acta Mater. 68 (2014) 279–294.

[3]   N. Reznikov, R. Shahar, S. Weiner, Bone hierarchical structure in three dimensions, Acta Biomater. 10 (2014) 3815–3826.

[4]   N. Reznikov, M. Bilton, L. Lari, M. Stevens, R. Kröger, Fractal-like hierarchical organization of bone begins at the nanoscale, Science 360 (2018). https://doi.org/10.1126/science.aao2189.

[5]   H. Schwarcz, E. McNally, G. Botton, A. Valente, The ultrastructure of bone as revealed in electron microscopy of ion-milled sections, Semin. Cell Dev. Biol. 46 (2015) 44–50. https://doi.org/10.1016/j.semcdb.2015.06.008.

[6]   J.D. Currey, Bones - Structure and mechanics, Princeton University Press, 2002. https://doi.org/10.1515/9781400849505.

[7]   B.M. Willie, E.A. Zimmermann, I. Vitienes, R.P. Main, S. V Komarova, Bone adaptation: Safety factors and load predictability in shaping skeletal form, Bone 131 (2020) 115114. https://doi.org/10.1016/j.bone.2019.115114.

[8]   P. Fratzl, R. Weinkamer, Nature's hierarchical materials, Prog. Mater. Sci. 52 (2007) 1263–1334. https://doi.org/https://doi.org/10.1016/j.pmatsci.2007.06.001.

[9]   R.K. Nalla, J.H. Kinney, R.O. Ritchie, Mechanistic fracture criteria for the failure of human cortical bone, Nat. Mater. 2 (2003) 164–168. https://doi.org/10.1038/nmat832.

[10]   H. Peterlik, P. Roschger, K. Klaushofer, P. Fratzl, From brittle to ductile fracture of bone, Nat. Mater. 5 (2006) 52–55. https://doi.org/10.1038/nmat1545.

[11]   J. Seto, H. Gupta, P. Zaslansky, D. Wagner, P. Fratzl, Tough Lessons From Bone: Extreme Mechanical Anisotropy at the Mesoscale, Adv. Funct. Mater. 18 (2008) 1905–1911. https://doi.org/10.1002/adfm.200800214.

[12]   M.E. Launey, M.J. Buehler, R.O. Ritchie, On the mechanistic origins of toughness in bone, Annu. Rev. Mater. Res. 40 (2010) 25–53.

[13]   J.D. Currey, R. Shahar, Cavities in the compact bone in tetrapods and fish and their effect on mechanical properties, J. Struct. Biol. 183 (2013) 107–122. https://doi.org/10.1016/j.jsb.2013.04.012.

[14]   S. Bolamperti, I. Villa, A. Rubinacci, Bone remodeling: an operational process ensuring survival and bone mechanical competence, Bone Res. 10 (2022) 48. https://doi.org/10.1038/s41413-022-00219-8.

[15]   A. G Robling, C. H Turner, Mechanical signaling for bone modeling and remodeling, Crit. Rev. Eukaryot. Gene Expr. 19 (2009) 319–338.

[16]   L.F. Bonewald, The Amazing Osteocyte, in: J. Bone Miner. Res., 2011.

[17]   S. Weinbaum, S.C. Cowin, Y. Zeng, A model for the excitation of osteocytes by mechanical loading-induced bone fluid shear stresses, J. Biomech. 27 (1994) 339–360. https://doi.org/https://doi.org/10.1016/0021-9290(94)90010-8.

[18]   P. Buenzli, N. Sims, Quantifying the osteocyte network in the human skeleton, Bone 75 (2015) 144–150. https://doi.org/10.1016/j.bone.2015.02.016.

[19]   A. Kolliker, On the different types in the microscopic structure of the skeleton of osseous fishes, Proc. R. Soc. London 9 (1857) 656–668. http://www.jstor.org/stable/111566.

[20]   L. Ofer, M. Dumont, A. Rack, P. Zaslansky, R. Shahar, New insights into the process of osteogenesis of anosteocytic bone, Bone 125 (2019) 61–73.

[21]   D. Davesne, F.J. Meunier, A.D. Schmitt, M. Friedman, O. Otero, R.B.J. Benson, The phylogenetic origin and evolution of acellular bone in teleost fishes: insights into osteocyte function in bone metabolism, Biol. Rev. Camb. Philos. Soc. 94 (2019) 1338–1363. https://doi.org/10.1111/BRV.12505.

[22]   P.E. Witten, A. Huysseune, A comparative view on mechanisms and functions of skeletal remodelling in teleost fish, with special emphasis on osteoclasts and their function, Biol. Rev. 84 (2009) 315–346.

[23] P. E. Witten, B. K. Hall, Teleost Skeletal Plasticity: Modulation, Adaptation, and Remodelling, Copeia 103 (2015) 727–739.

[24] A. Atkins, J. Milgram, S. Weiner, R. Shahar, The response of anosteocytic bone to controlled loading, J. Exp. Biol. 218 (2015) 3559–3569.

[25] A. Atkins, M.N. Dean, M.L. Habegger, P.J. Motta, L. Ofer, F. Repp, A. Shipov, S. Weiner, J.D. Currey, R. Shahar, Remodeling in bone without osteocytes: Billfish challenge bone structure–function paradigms, Proc. Natl. Acad. Sci. 111 (2014) 16047–16052. https://doi.org/10.1073/pnas.1412372111.

[26] K. Sauer, A. Rack, H.A. Mustafa, M. Thiele, R. Shahar, P. Zaslansky, Microstructure and texture contributing to damage resistance of the anosteocytic hinge-bone in the cleithrum of Esox lucius, Int. J. Mater. Res. 111 (2020) 78–85. https://doi.org/10.3139/146.111801/.

[27] M.W. Westneat, A.M. Olsen, How fish power suction feeding, Proc. Natl. Acad. Sci. 112 (2015) 8525–8526. https://doi.org/10.1073/pnas.1510522112.

[28] D.G. Harper, R.W. Blake, Prey capture and the fast-start performance of northern pike Esox lucius, J. Exp. Biol. 155 (1991) 175–192. https://doi.org/10.1242/jeb.155.1.175.

[29] D.G. Harper, R.W. Blake, Fast-start performance of rainbow trout Salmo gairdneri and northern pike Esox lucius, J. Exp. Biol. 150 (1990) 321–342.

[30] S.W. Day, T.E. Higham, R. Holzman, S. Van Wassenbergh, Morphology, Kinematics, and Dynamics: The mechanics of suction feeding in fishes, Integr. Comp. Biol. 55 (2015) 21–35. https://doi.org/10.1093/icb/icv032.

[31] C. Schneider, W. Rasband, K. Eliceiri, NIH Image to ImageJ: 25 years of image analysis, Nat. Methods 9 (2012) 671.

[32] D. Paganin, S.C. Mayo, T.E. Gureyev, P.R. Miller, S.W. Wilkins, Simultaneous phase and amplitude extraction from a single defocused image of a homogeneous object, J. Microsc. 206 (2002) 33–40.

[33] A. Mirone, E. Brun, E. Gouillart, P. Tafforeau, J. Kieffer, The PyHST2 hybrid distributed code for high speed tomographic reconstruction with iterative reconstruction and a priori knowledge capabilities, Nucl. Instruments Methods Phys. Res. Sect. B Beam Interact. with Mater. Atoms 324 (2014) 41–48.

[34] I. Zlotnikov, V. Schoeppler, Thermodynamic aspects of molluscan shell ultrastructural morphogenesis, Adv. Funct. Mater. 27 (2017) 1700506.

[35] A. Khimchenko, C. Bikis, A. Pacureanu, S.E. Hieber, P. Thalmann, H. Deyhle, G. Schweighauser, J. Hench, S. Frank, M. Müller-Gerbl, G. Schulz, P. Cloetens, B. Müller, Hard X-Ray Nanoholotomography: Large-Scale, Label-Free, 3D Neuroimaging beyond Optical Limit, Adv. Sci. 5 (2018) 1700694. https://doi.org/10.1002/advs.201700694.

[36] P. Kirkpatrick, A. V Baez, Formation of optical images by X-Rays, J. Opt. Soc. Am. 38 (1948) 766–774.

[37] L.C.U. Junqueira, G. Bignolas, R.R. Brentani, Picrosirius staining plus polarization microscopy, a specific method for collagen detection in tissue sections, Histochem. J. 11 (1979) 447–455.

[38] W. De Nolf, F. Vanmeert, K. Janssens, □□□□: crystalline phase distribution maps by two-dimensional scanning and tomographic (micro) X-ray powder diffraction, J. Appl. Crystallogr. 47 (2014) 1107–1117.

[39] K. Sauer, I. Zizak, J.B. Forien, A. Rack, E. Scoppola, P. Zaslansky, Primary radiation damage in bone evolves via collagen destruction by photoelectrons and secondary emission self-absorption, Nat. Commun. 13 (2022) 1–12. https://doi.org/10.1038/s41467-022-34247-z.

[40] H. Spatz -Ch., E.J. O'Leary, J.F.V. Vincent, Young's moduli and shear moduli in cortical bone, Proc. R. Soc. London. Ser. B Biol. Sci. 263 (1996) 287–294. https://doi.org/10.1098/RSPB.1996.0044.

[41] M.A. Sutton, J.-J. Orteu, H.W. Schreier, Image correlation for shape, motion and deformation measurements, Springer, 2009.

[42] B. Pan, H. Xie, Z. Wang, K. Qian, Z. Wang, Study on subset size selection in digital image correlation for speckle patterns, Opt. Express 16 (2008) 7037–7048.

[43] R. Harilal, M. Ramji, Adaptation of open source 2D DIC software Ncorr for solid mechanics applications, in: Adapt. Open Source 2D DIC Softw. Ncorr Solid Mech. Appl., 2014. https://doi.org/10.13140/2.1.4994.1442.

[44] M. Langer, A. Pacureanu, H. Suhonen, Q. Grimal, P. Cloetens, F. Peyrin, X-Ray phase nanotomography resolves the 3D human bone ultrastructure, PLoS One 7 (2012) 1–7.

[45] J.D. Currey, M.N. Dean, R. Shahar, Revisiting the links between bone remodelling and osteocytes: insights from across phyla, Biol. Rev. 92 (2017) 1702–1719. https://doi.org/10.1111/BRV.12302.

[46] G.P. Evans, J.C. Behiri, J.D. Currey, W. Bonfield, Microhardness and Young's modulus in cortical bone exhibiting a wide range of mineral volume fractions, and in a bone analogue, J. Mater. Sci. Mater. Med. 1 (1990) 38–43.

[47] D.J. Daegling, J.L. Hotzman, W.S. McGraw, A.J. Rapoff, Material property variation of mandibular symphyseal bone in colobine monkeys, J. Morphol. 270 (2009) 194–204. https://doi.org/10.1002/JMOR.10679.

[48] C.H. Turner, T. Wang, D.B. Burr, Shear strength and fatigue properties of human cortical bone determined from pure shear tests, Calcif. Tissue Int. 69 (2001) 373–378. https://doi.org/10.1007/S00223-001-1006-1.

[49] J.J. Kruzic, R.O. Ritchie, Fatigue of mineralized tissues: Cortical bone and dentin, J. Mech. Behav. Biomed. Mater. 1 (2008) 3–17. https://doi.org/10.1016/J.JMBBM.2007.04.002.

[50] M.A. Rashid, M.A. Mansur, P. Paramasivam, Correlations between Mechanical Properties of High-Strength Concrete, J. Mater. Civ. Eng. 14 (2002) 230–238. https://doi.org/10.1061/(ASCE)0899-1561(2002)14:3(230).

[51] D.J. Hannant, S.B. Venkata Siva, P.S. Rama Sreekanth, 5.15 Cement-Based Composites☆, in: P.W.R. Beaumont, C.H. Zweben (Eds.), Compr. Compos. Mater. II, Elsevier, Oxford, 2018: pp. 379–420. https://doi.org/https://doi.org/10.1016/B978-0-12-803581-8.03903-5.

[52] Tempered glass, Nature 31 (1885) 413–414. https://doi.org/10.1038/031413B0.

[53] H. Ping, W. Wagermaier, N. Horbelt, E. Scoppola, C. Li, P. Werner, Z. Fu, P. Fratzl, Mineralization generates megapascal contractile stresses in collagen fibrils, Science (80-.). 376 (2022) 188–192. https://doi.org/10.1126/science.abm2664.

[54] Robert Humble, Connecting rod, 1888. https://patents.google.com/patent/US391148A/en.

[55] A. Atkins, N. Reznikov, L. Ofer, A. Masic, S. Weiner, R. Shahar, The three-dimensional structure of anosteocytic lamellated bone of fish, Acta Biomater. 13 (2015) 311–323.

[56] P. Fratzl, H.S. Gupta, F.D. Fischer, O. Kolednik, Hindered crack propagation in materials with periodically varying Young's modulus—Lessons from biological materials, Adv. Mater. 19 (2007) 2657–2661.

[57] H. Chai, J.J.-W. Lee, P.J. Constantino, P.W. Lucas, B.R. Lawn, Remarkable resilience of teeth, Proc. Natl. Acad. Sci. 106 (2009) 7289–7293.

[58] L. Cohen, M. Dean, A. Shipov, A. Atkins, E. Monsonego-Ornan, R. Shahar, Comparison of structural, architectural and mechanical aspects of cellular and acellular bone in two teleost fish, J. Exp. Biol. 215 (2012) 1983–1993.

[59] J. Zaretsky, S. Griess-Fishheimer, A. Carmi, T. Travinsky Shmul, L. Ofer, T. Sinai, S. Penn, R. Shahar, E. Monsonego-Ornan, Ultra-processed food targets bone quality via endochondral ossification, Bone Res. 9 (2021) 14. https://doi.org/10.1038/s41413-020-00127-9.

[60] A. Shipov, G. Segev, H. Meltzer, M. Milrad, O. Brenner, A. Atkins, R. Shahar, The Effect of Naturally Occurring Chronic Kidney Disease on the Micro-Structural and Mechanical Properties of Bone, PLoS One 9 (2014) e110057. https://doi.org/10.1371/journal.pone.0110057.

[61] C.M. Heveran, J.D. Boerckel, Osteocyte remodeling of the lacunar-canalicular system: What's in a name?, Curr. Osteoporos. Rep. 21 (2023) 11–20. https://doi.org/10.1007/s11914-022-00766-3.

[62] S. Lees, E.A. Page, A study of some properties of mineralized turkey leg tendon, Connect. Tissue Res. 28 (1992) 263–287. https://doi.org/10.3109/03008209209016820.

[63] W. Landis, F. Silver, The structure and function of normally mineralizing avian tendons, Comp. Biochem. Physiol. A. Mol. Integr. Physiol. 133 (2002) 1135–1157. https://doi.org/10.1016/s1095-6433(02)00248-9.

[64] S. Lees, K.S. Prostak, V.K. Ingle, K. Kjoller, The loci of mineral in turkey leg tendon as seen by atomic force microscope and electron microscopy, Calcif. Tissue Int. 55 (1994) 180–189. https://doi.org/10.1007/BF00425873.

[65] V. Burgio, M. Civera, M. Rodriguez, E. Pizzolante, S. Prezioso, A. Bertuglia, C. Surace, Mechanical properties of animal tendons: A review and comparative study for the identification of the most suitable human tendon surrogates, Processes 10 (2022) 485. https://doi.org/10.3390/pr10030485.

[66] T.A.L. Wren, S.A. Yerby, G.S. Beaupré, D.R. Carter, Mechanical properties of

the human achilles tendon, Clin. Biomech. 16 (2001) 245–251.
https://doi.org/https://doi.org/10.1016/S0268-0033(00)00089-9.

[67] M. Abrahams, Mechanical behaviour of tendonIn vitro, Med. Biol. Eng. 5 (1967)
433–443. https://doi.org/10.1007/BF02479137.

[68] A. Matson, N. Konow, S. Miller, P. Konow, T. Roberts, Tendon material
properties vary and are interdependent among turkey hindlimb muscles, J. Exp.
Biol. 215 (2012) 3552–3558. https://doi.org/10.1242/jeb.072728.

[69] I.A.K. Fiedler, O. Elmogazy, G. Courtemanche, L. Cardoso, J.P. Berteau,
Bones of teleost fish demonstrate high fracture strain, J. Biomech. 120 (2021)
110341. https://doi.org/https://doi.org/10.1016/j.jbiomech.2021.110341.

[70] R.M. Alexander, Elastic energy stores in running vertebrates, Am. Zool. 24
(1984) 85–94.

[71] X. Zhao, Y. Zhu, Z. Zhu, Y. Liang, Y. Niu, J. Lin, Characterization, Dissolution,
and Solubility of Zn-Substituted Hydroxylapatites [(Zn x Ca 1− x) 5 (PO 4) 3
OH] at 25°C, J. Chem. 2017 (2017) 1–13.
https://doi.org/10.1155/2017/4619159.

[72] F. Ren, R. Xin, X. Ge, Y. Leng, Characterization and structural analysis of zinc-
substituted hydroxyapatites, Acta Biomater. 5 (2009) 3141–3149.
https://doi.org/10.1016/J.ACTBIO.2009.04.014.

[73] B. Pemmer, A. Roschger, A. Wastl, J. Hofstaetter, P. Wobrauschek, R. Simon,
H. Thaler, P. Roschger, K. Klaushofer, C. Streli, Spatial Distribution of the
Trace Elements Zinc, Strontium and Lead in Human Bone Tissue., Bone 57
(2013). https://doi.org/10.1016/j.bone.2013.07.038.

[74] J. D. Currey, Safety Factors and Scaling Effects in Bones, The Mechanical
Adaptation of Bones, Princeton University Press 2014.
https://doi.org/10.1515/9781400853724.

[75] J.M. Horton, A.P. Summers, The material properties of acellular bone in a
teleost fish, J. Exp. Biol. 212 (2009) 1413–1420.

[76] A. Silveira, N. Kardjilov, H. Markötter, E. Longo, I. Greving, P. Lasch, R.
Shahar, P. Zaslansky, Water flow through bone: Neutron tomography reveals
differences in water permeability between osteocytic and anosteocytic bone
material, Mater. Des. 224 (2022) 111275.
https://doi.org/https://doi.org/10.1016/j.matdes.2022.111275.

[77] R. Nanda, S. Hazan, K. Sauer, V. Aladin, K. Keinan-Adamsky, B. Corzilius, R.
Shahar, P. Zaslansky, G. Goobes, Molecular differences in collagen
organization and in organic-inorganic interfacial structure of bones with and
without osteocytes, Acta Biomater. 144 (2022) 195–209.
https://doi.org/https://doi.org/10.1016/j.actbio.2022.03.032.

[78] J.-B. Forien, I. Zizak, C. Fleck, A. Petersen, P. Fratzl, E. Zolotoyabko, P.
Zaslansky, Water-mediated collagen and mineral nanoparticle interactions
guide functional deformation of human tooth dentin, Chem. Mater. 28 (2016)
3416–3427.

[79] J.D. Almer, S.R. Stock, Micromechanical response of mineral and collagen

phases in bone, J. Struct. Biol. 157 (2007) 365–370.
https://doi.org/https://doi.org/10.1016/j.jsb.2006.09.001.

[80] S.R. Stock, F. Yuan, L.C. Brinson, J.D. Almer, Internal strain gradients
      quantified in bone under load using high-energy X-ray scattering, J. Biomech.
      44 (2011) 291–296.
      https://doi.org/https://doi.org/10.1016/j.jbiomech.2010.10.015.

[81] L. Pannarale, P. Braidotti, L. d'Alba, E. Gaudio, Scanning Electron Microscopy
      of Collagen Fiber Orientation in the Bone Lamellar System in Non-Decalcified
      Human Samples, Cells Tissues Organs 151 (1994) 36–42.

[82] M.-M. Giraud-Guille, L. Besseau, R. Martin, Liquid crystalline assemblies of
      collagen in bone and in vitro systems, J. Biomech. 36 (2003) 1571–1579.

[83] J.Y. Rho, S.R. Mishra, K. Chung, J. Bai, G.M. Pharr, Relationship Between
      Ultrastructure and the Nanoindentation Properties of Intramuscular Herring
      Bones, Ann. Biomed. Eng. 29 (2001) 1082–1088.

[84] A.J. Bushby, V.L. Ferguson, A. Boyde, Nanoindentation of bone: Comparison
      of specimens tested in liquid and embedded in polymethylmethacrylate, J.
      Mater. Res. 19 (2004) 249–259.

Statement of Significance

By combining structural and mechanical characterization techniques spanning the mm to the sub-nanometer length scales, this work provides insights into the structural organization and properties of a resilient bone found in pike fish. Our observations show how the anosteocytic bone within the pectoral gridle of these fish, lacking any biological (remodeling) repair mechanisms, is adapted to sustain natural repeated loading cycles of abrupt jaw-gaping and swallowing. We find residual strains within the mineral apatite nano-crystals that contribute to forming a remarkably resilient composite material. Such information gleaned from bony structures that are different from the usual bones of mammals showcases how nature incorporates smart features that induce damage tolerance in bone material, an adaptation acquired through natural evolutionary processes.

Graphical Abstract
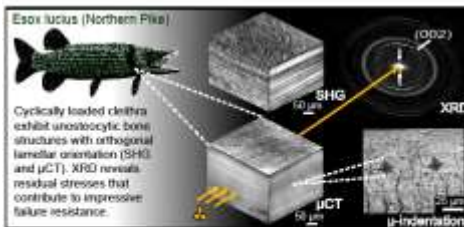
Declaration of interests

☒ The authors declare that they have no known competing financial interests or personal relationships that could have appeared to influence the work reported in this paper.

☐The authors declare the following financial interests/personal relationships which may be considered as potential competing interests: